

Identification of Background False Positives from *Kepler* Data

Stephen T. Bryson¹, Jon M. Jenkins², Ronald L. Gilliland³, Joseph D. Twicken²,
Bruce Clarke², Jason Rowe², Douglas Caldwell², Natalie Batalha^{1,4}, Fergal Mullally²,
Michael R. Haas¹, Peter Tenenbaum²

ABSTRACT

The *Kepler Mission* was launched on March 6, 2009 to perform a photometric survey of more than 100,000 dwarf stars to search for terrestrial-size planets with the transit technique. The reliability of the resulting planetary candidate list relies on the ability to identify and remove false positives. Major sources of astrophysical false positives are planetary transits and stellar eclipses on background stars. We describe several new techniques for the identification of background transit sources that are separated from their target stars, indicating an astrophysical false positive. These techniques use only Kepler photometric data. We describe the concepts and construction of these techniques in detail as well as their performance and relative merits.

Subject headings: Extrasolar Planets, Data Analysis and Techniques, Kepler Telescope

1. Introduction

The *Kepler* mission is designed to determine the frequency of Earth-size planets in and near the habitable zone of solar-like stars via the detection of photometric transits (Borucki, et al. 2010a; Koch, et al. 2010a). *Kepler* surveys more than 100,000 late-type

¹NASA Ames Research Center, Moffett Field, CA 94035; steve.bryson@nasa.gov

²SETI Institute/NASA Ames Research Center, Moffett Field, CA 94035

³Center for Exoplanets and Habitable Worlds, The Pennsylvania State University, University Park, PA 16802

⁴Department of Physics and Astronomy, San Jose State University, San Jose, CA 95192

dwarf stars in the solar neighborhood with visual magnitudes between 8 and 16 for > 4 years looking for transits of planets around those stars. There are several astrophysical phenomena that can cause a false-positive detection that mimics a planetary transit on a target star. Approximately 40% of the transit-like signals detected by *Kepler* that have been deemed *Kepler* Objects of Interest (KOIs) have been determined to be due to false positives.

To increase the reliability of the determination which KOIs are planetary candidates, it is important to identify as many of these false-positives as possible. Many KOIs have transit signals that are too small for conventional ground-based followup, so false-positive identification has to be based on *Kepler* data alone. This paper describes several distinct but complimentary methods for using *Kepler* data to detect cases where the source of a transit-like event is offset from the target star’s position on the sky. These background false positives make up a substantial fraction of all false positives, with most of the other false positives being due to grazing eclipsing stellar companions associated with the target star. At low Galactic latitudes, *background false positives* account for almost 40% of all *Kepler* transit-like signals, with the fraction dropping to about 10% at high Galactic latitudes (see Figure 1). Background false positives are detected in *Kepler* data by observing that the pixels that change during the transit are distinct from the target star’s pixels. Such cases are referred to as *active pixel offsets* (APOs). The methods described in this paper cannot detect all background transit sources: for example when the transit source is extremely close to the target star on the sky, but they can identify a large percentage of background false positives.

The techniques described in this paper rely on pixel data returned from the *Kepler* spacecraft. Without this pixel data the identification of background transit sources is much more difficult. Indeed, for dim target stars or for small planets with low SNR transits, ground-based followup typically will not suffice to identify background false positives. In such cases, background false positive identification would be impossible using stellar light curves alone. Without the pixels, the star hosting the transit signal cannot be determined. Without knowing the star hosting the transit, the object causing the transit cannot be characterized. Therefore the availability of the pixel data used to create the stellar light curves is a critical component of the success of any transit survey. This insight should drive the design of future transit survey missions.

In the rest of this section we discuss background false positives in general, their identification via pixel analysis and how that identification is used in the vetting of *Kepler* planet candidates. The bulk of this paper describes several techniques for performing pixel-level analysis to identify background false positives. In §2 we describe the photometric centroid technique, and in §3 the use of difference images to localize the transit signal source. Pixel

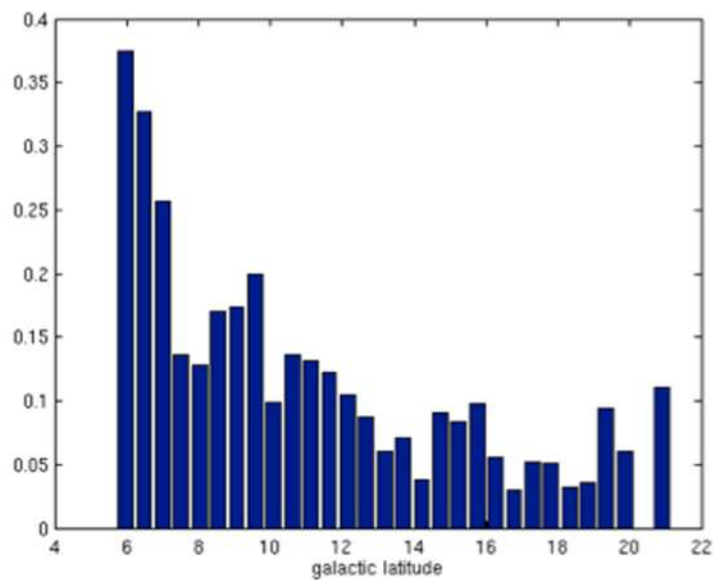


Fig. 1.— The distribution of the fraction of transit signal sources that are offset from the target star, indicating a background false positive. For low Galactic latitude almost 40% of all *Kepler* KOIs are background false positives, while for mid to high Galactic latitudes the fraction drops to about 10%. This figure is based on data from Batalha, et al. (2012).

correlations are described in §4. We briefly address the special case of saturated targets in §5. §6 presents several perspectives on how well these techniques perform, with special emphasis on comparing the photometric centroid and difference image techniques.

Throughout this paper we use several examples identified as *Kepler* objects of interest (KOIs) (Borucki, et al. 2011a,b; Batalha, et al. 2010a, 2012; Burke, et al. 2013). Some KOIs are now valid candidates, while others have been determined to be false positives. We give particular attention to two examples to illustrate our techniques: KOI-221, which is a *Kepler* target where the transit source location is observationally coincident with the target, and KOI-109, which is a *Kepler* target for which the transit source is clearly offset from the target star. The list of KOIs and their properties can be found at the NASA Exoplanet Archive¹ while the light curves and pixel data for all *Kepler* targets can be found at the Mikulski Archive for Space Telescopes².

1.1. Background False Positives

There are several astrophysical phenomena that can mimic a planetary transit on a specified target star. Brown (2003) distinguishes 12 combinations of giant planets and stars in eclipsing and transiting systems that can produce light curves mimicking a planet transiting a solitary primary star. Six of the combinations do not involve planets at all, and four others distort the transit light curve so that the size of the planet is indeterminate.

In this paper we are concerned with those phenomena which are due to astrophysical sources that are not associated with the target star. These primarily include eclipsing binaries or large planet transits on stars that have flux in the pixels used to create the target star’s light curve. Because of dilution from the target star, even deep background eclipsing binaries often cannot be identified from the target star’s light curve alone. Analysis at the pixel level is required to identify the location of the transit signal source. We are particularly interested in cases where the transit signal’s source is sufficiently separated from the target star that we can measure a statistically significant offset between the target star and the transit source.

Additional sources of false positives that can be detected by the methods described in this paper include

- Very wide multiple star systems, where the transit source is gravitationally bound

¹<http://exoplanetarchive.ipac.caltech.edu>

²<http://archive.stsci.edu/kepler>

to the target star. When the separation between the target star and the companion hosting the transit signal source is large enough the methods described in this paper can detect the offset.

- Optical ghosts and electronic crosstalk (Caldwell, et al. 2010) from planetary transits or eclipsing binaries elsewhere on the *Kepler* focal plane. When the image of the ghost or crosstalk falls on the target star’s pixels but is sufficiently separated from the target star these sources can be detected by the methods described in this paper. In addition, optical ghosts can have very non-stellar morphologies. Transit signals due to optical ghosts will exhibit these morphologies in several of the techniques described in this paper.

Our basic strategy is to measure the location of the transit source on the sky, compare that to the location of the target star, and declare the transit signal a false positive if the transit source location is significantly offset (more than three standard deviations, written $> 3\sigma$) from the target star location based on reliable data. All the methods of computing these offsets described in this paper use χ^2 minimizing (least-squares) methods. Assuming Gaussian statistics, these offsets form a two-degree-of-freedom χ^2 distribution, that have offsets $> 3\sigma$ due to random fluctuations about 1.11% of the time. As we will show in this paper, offset uncertainties follow an approximately Gaussian distribution in a statistical sense, through the uncertainty around individual targets may not be Gaussian.

1.2. Pixel Analysis to Identify the Location of the Transit Source

As mentioned in Section 1.1, the background binary causing a transit signal can be very faint, indeed significantly fainter than the general background or the wings of the target star, and still mimic a planetary transit. Consider the case of an aperture that contains only a target star with constant flux F and a background binary with other negligible sky background. If the background binary is Δm magnitudes fainter than the target star, then the flux ratio of the background star to the target star is $\Delta F = (100)^{-\Delta m/5}$. If the background binary has a fractional eclipse depth d_{back} , then the total flux out of transit is $F^{\text{out}} = F + F\Delta F$. In transit the total flux is $F^{\text{in}} = F + (1 - d_{\text{back}})F\Delta F$. Therefore the fractional observed depth in the aperture is

$$d_{\text{obs}} = 1 - \frac{F^{\text{in}}}{F^{\text{out}}} = 1 - \frac{1 + (1 - d_{\text{back}})\Delta F}{1 + \Delta F} = \frac{d_{\text{back}}\Delta F}{1 + \Delta F}.$$

In the case of a 14th magnitude target star and a 22nd magnitude background eclipsing binary with $d_{\text{back}} = 0.5$ we get $d_{\text{obs}} = 315$ ppm. A transit of this depth is easily detected

in *Kepler* data and would mimic the transit of a small planet, though the 22nd magnitude background star would not be readily apparent in the *Kepler* data.

There are several ways to use *Kepler* pixel data to measure the distance from the target star to the transit source. We focus on three classes of techniques, each of which have their strengths and weaknesses. As we describe in detail below, none of these techniques work well in all circumstances due to systematic error sources that vary from technique to technique, but we find that the combination of these techniques covers the majority of cases where there is sufficiently large signal to noise ratio (SNR) to measure the transit source location. Our focus is on techniques that can be reliably automated due to the large number of objects in the *Kepler* data. We would also, when possible, like to associate the transit source with a known star. Therefore we describe techniques that provide an estimate of the transit source location on the sky rather than simply determining if the transit source is at the target star location.

Kepler collects pixels specific to each target (Bryson, et al. 2010). A subset of these pixels, called the photometric optimal aperture, is summed to create the light curve for the target (see Figure 2). The pixel analysis in this paper uses either the optimal aperture plus one halo of pixels, defined as any pixel adjacent to the optimal aperture (the photometric centroid technique described in §2), or all pixels collected for a target (the difference image technique described in §3). For most targets, *Kepler* pixel data is collected once every *long cadence* (29.4 minutes), and for a subset of targets data is collected once every *short cadence* (0.98 minutes). In this paper we limit our discussion to long cadence observations.

All of the methods described in this paper identify spatially separated false positives by comparing pixel values during in-transit cadences to values of the same pixels during out-of-transit cadences.

Analysis of *Kepler* pixels to identify the location of the transit relative to the target star has to solve three problems:

- **Analyzing the Pixels Within a Cadence** There are various ways that the transit source location can be inferred from pixel data. Some of these methods require the identification of cadences that occur during transit and cadences that do not.
- **Combining the Cadences Within a Quarter** The *Kepler* spacecraft rotates 90 degrees about the photometer boresite every ~ 93 days (Koch, et al. 2010a). Each ~ 93 day period is referred to as a Quarter. While the *Kepler* focal plane is approximately symmetric under these 90 degree rolls, a star falls on different CCD chips at different pixel coordinates in different quarters. How in-transit and out-of-transit cadences within a quarter are selected and combined varies from technique to technique.

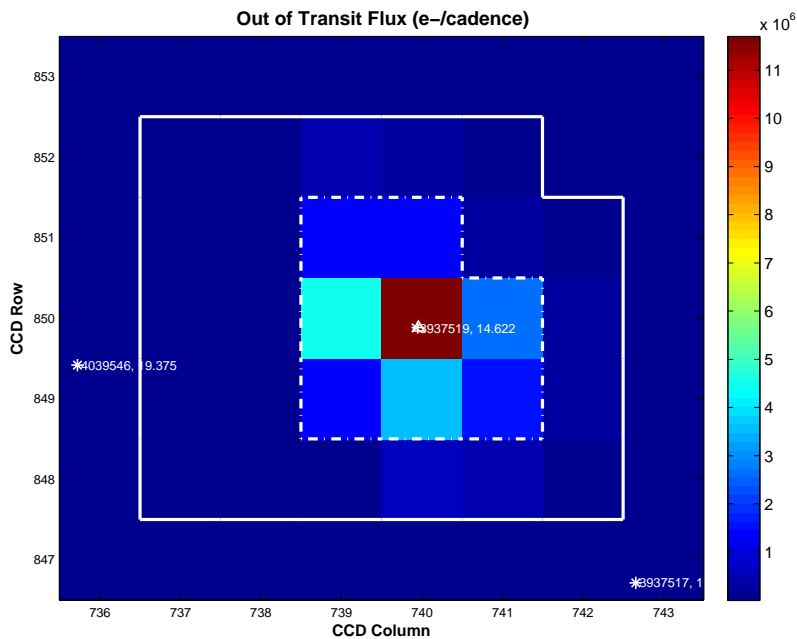


Fig. 2.— Pixels collected for a *Kepler* target. All collected pixels are outlined by the solid white line. The photometric optimal aperture is outlined with a white dot-dashed line. The pixel values are shown by the pixel color. Asterisks give the location of known stars in the field, including those just outside the collected pixels. For each star the Kepler Input Catalog number and Kepler magnitude are given.

- **Combining the Cadences Across Quarters** Some of the techniques we discuss operate within a single quarter and will deliver different results from quarter to quarter. These results for each quarter must be combined to provide an overall measurement.

There are three classes of methods that we use to solve these problems:

- **Photometric Centroid Shift** Detection of a shift in the photometric centroid of the flux in the pixels (see §2) that is correlated with the transit signal. This centroid shift can be used to estimate the location of the transit source as described in §2.
- **Difference Imaging** By constructing the difference of the in- and out-of-transit pixel images, a direct image of the transit source can be constructed as described in §3. The centroid of this image provides a direct measurement of the location of the transit source. This method assumes that the only source of flux variation is the object creating the transit signal.
- **Pixel Correlation Images** When the transit signal can be detected in individual pixels via correlation with the photometric transit signal, an image can be constructed where the value of each pixel is given the correlation value as described in §4. This is an alternative method of creating a direct image of the transit source, whose centroid provides the transit source location.

These three methods are in principle very similar, but have different responses to systematics and noise, transit SNR, and field crowding. The use of all three methods provides increased sensitivity and confidence in the identification of background false positives, particularly when the transit SNR is low.

1.3. The Role of Offset Analysis in Planet Candidate Vetting

The techniques described in this paper are used to decide whether or not a detected transit signal belongs on the *Kepler* planetary candidate list. The details of how these analyses are used has evolved over time, and are described in papers detailing the release of planetary candidate lists (Borucki, et al. 2010a, 2011a,b; Batalha, et al. 2012; Burke, et al. 2013). The general pattern is to identify those targets that show a significant offset between the target star and the transit source relying primarily on the difference imaging method. Those targets that have a borderline significant source offset or have other cause for concern are examined using all the methods described in this paper, including manual examination

of the pixels. Targets that have a confirmed offset from the transit source are identified as false positives. This disposition has changed over time for a small number of targets, as the techniques described in this paper have become more refined and as more data becomes available, resulting in greater measurement precision.

2. Source Location from Photometric Centroid Shifts

2.1. Computing Pixel Centroids

The most traditional method for estimating the position of a light source is that of photometric centroids, also known as flux-weighted centroids. Photometric centroids measure the “center of light” of all flux in the pixels. While photometric centroids do not exactly measure the location of any particular star, it will be shown below that under idealized circumstances they can be used to compute the location of a transit source.

The row and column photometric centroids of the pixels for each target are computed for each cadence as

$$C_{\text{row}} = \frac{\sum_{j=1}^N r_j b_j}{\sum_{j=1}^N b_j}, \quad C_{\text{column}} = \frac{\sum_{j=1}^N c_j b_j}{\sum_{j=1}^N b_j} \quad (1)$$

where b_j is the flux in pixel j at row and column (r_j, c_j) . If we denote the covariance matrix of the pixel values b_j as \mathcal{C}_{ij} (so the uncertainties in the pixel values are the square root of the diagonals: $\sigma_j = \sqrt{\mathcal{C}_{jj}}$), then the standard propagation of errors gives the uncertainty in the photometric row centroid as

$$\sigma_{C_{\text{row}}} = \sqrt{\frac{\sum_{j=1}^N \sum_{i=1}^N r_i \mathcal{C}_{ij} r_j}{\left(\sum_{j=1}^N b_j\right)^2} + \frac{\left(\sum_{j=1}^N r_j b_j\right)^2}{\left(\sum_{j=1}^N b_j\right)^4} \sum_{i=1}^N \sum_{j=1}^N \mathcal{C}_{ij}} \quad (2)$$

with a similar formula for the uncertainty in the column centroid. We see that the sensitivity of the centroid value $\sigma_{C_{\text{row}}}$ is proportional to the square root of the elements of the covariance matrix \mathcal{C}_{ij} , in particular to the uncertainty in the pixel values σ_j , divided by the total flux in the pixels $\sum_{j=1}^N b_j$. Therefore, photometric centroids are very sensitive to variations in pixel value, in particular to shot noise and stellar variability.

For photometric centroids computed in the *Kepler* pipeline, j ranges over the optimal aperture plus a single ring of pixels (sometimes called a *halo*). The result is a time series containing the row and column centroids, called *centroid time series*. The centroid shift is

defined as the centroid value for cadences out of transit, C^{out} , subtracted from the centroid value for cadences in transit C^{in} : $\Delta C = C^{\text{in}} - C^{\text{out}}$. We assume shifts in different cadences are uncorrelated, so these shifts have an uncertainty given by $\sigma_{\Delta C}^2 = \sigma_{C^{\text{in}}}^2 + \sigma_{C^{\text{out}}}^2$.

It is very important to distinguish between the *centroid shift*, which measures how far the centroid moves between in- and out-of-transit cadences, and the *source offset*, which measures the separation of the target star from the transit source. As we will describe below, the centroid shift and source offset are related, but measure very different things. The centroid shift measures the change in the photometric centroid due to all changes in flux in the aperture. The source offset is derived from the centroid shift, but measures the separation between the target star and the transit source (which may or may not be a different star). In particular, because there is always background flux and field stars, the centroid shift ΔC will always be non-zero even when the transit signal is on the target star. In such cases the centroid shift can be relatively large while the source offset may be very close to zero.

Low-frequency secular trends due to small, slow changes such as differential velocity aberration, small pointing drifts and thermally induced focal length changes are common in centroid time series (Christiansen, et al. 2012). These trends are removed prior to the analysis described in this section, for example by local median filtering using a window of 48 cadences.

To facilitate combining the centroids across quarters, the centroid time series is converted to celestial right ascension (RA) and declination (Dec) using the *Kepler* focal plane geometry model in combination with motion polynomials that capture local variations in the focal plane geometry model (Tenenbaum and Jenkins 2010). In these coordinates the centroid shift ΔC is expressed as seconds of arc.

When the centroid shift ΔC is large enough, it can be taken to indicate that the transit source is not on the target star. Using ΔC directly to make this determination must be done with great care, however. ΔC will be smallest when the target star is the source of the transit, the target star is isolated, residual background flux is small after background correction, and the target star is near the geometric center of the centroided pixels. This is rarely the case, however, so even when the target star is the source of the transit there will be a non-trivial centroid shift. A larger centroid shift that is correlated with the time of transit is an indicator that the transit source may not be the target star. Determining whether a centroid shift indicates that the transit source is not the target star is difficult, however, and depends on the details of other flux sources in the target’s pixel aperture. In §2.3 we describe how to use the centroid shift to estimate the location of the source of the centroid signal, which is a more robust method for determining whether the transit source

is the target star than using the centroid shift alone.

A graphical method showing the correlation between the centroid shift and the transit signal is to plot the median-detrended centroid time series against the normalized, median-detrended light curve flux value. The results is a *cloud plot*, shown in Figure 3. Most points in a cloud plot are out-of-transit cadences and form a cluster around (0,0). The size of the cloud reflects the sensitivity of the photometric centroid computation to noise in the pixel values. When there is no centroid shift associated with transits, the points in transit (with negative normalized flux) fall directly below the out-of-transit points. When there is a centroid shift associated with the transit, points in transit will fall to the side of the out-of-transit cloud. Seeing sideways motion of the in-transit points as shown in the right panel of Figure 3 indicates a centroid shift associated with the transit. This suggests that the transit source may be offset from the target star. As explained above, care must be taken when interpreting cloud plots because there may be a non-trivial centroid shift correlated with the transit even when the target star is the transit source.

2.2. Correlating Centroid Motion with the Transit Model

The centroid time series is sensitive to photometric noise, so quantitatively measuring the correlation of the centroid shift with the photometric transit signal can be difficult, particularly for low SNR transits. A simple approach is to identify all in- and out-of-transit cadences, and compute the average (or median) in- and out-of-transit centroid values. The average centroid shift is then given by the difference of the in- and out-of-transit average centroid locations. This method encounters many difficulties, however: quarter-to-quarter differences in aperture shape will introduce systematic errors, and non-transit related variability will degrade these averages as measures of transit-related shifts. A better method is to fit a transit model computed during data validation (Wu, et al. 2010) to the centroid time series. This will provide a more robust measurement of ΔC .

In this section we define the centroid shift time series $\Delta C_n = C_n - C^{\text{out}}$ where C^{out} is the average out-of-transit centroid and n labels the cadence. In this section We assume that the transit model has been whitened to remove secular variations such as those due to pointing drift and stellar variability (Wu, et al. 2010), in which case the centroid shift time series ΔC_n must be whitened in the same way. We compute a least-squares fit of the centroid shift time series ΔC_n to the transit model M_n multiplied by a constant γ , weighted by the centroid uncertainties. This fit is most easily done by requiring that the transit model and the centroid shift time series both have zero mean when the transit is not occurring. This implies that the transit model $M_n = 0$ for out-of-transit cadences. When this is the case we

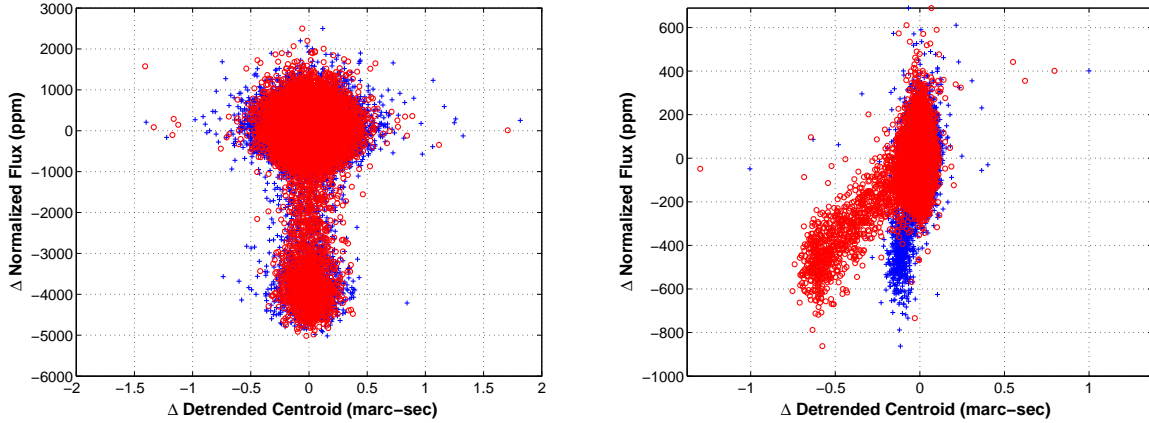


Fig. 3.— Example cloud plots where the normalized residual flux (y -axis) is plotted against the centroid shift (x -axis). Each point plots the normalized, median-detrended flux value against the median-detrended RA (blue crosses) or Dec (red circles) centroid time series in a single long cadence. In both figures most points are from out-of-transit cadences and form a cloud around (0,0). Left: When the transit is on an isolated target star (KOI-221 in this example), the centroid does not shift when in transit, so in-transit points are directly below the out-of-transit points. Right: When the transit is on an object offset from the target (KOI-109 in this example), the in-transit centroids are shifted relative to the out-of-transit centroids and appear below to one side, indicating a strong possibility of a background false positive. In this example the Dec centroid components show a shift while the RA components do not, indicating that the transit source is offset in the Dec direction.

minimize

$$\chi^2 = \sum_{n=1}^N \frac{1}{(\sigma_{\Delta C_n})^2} (\Delta C_n - \gamma M_n)^2. \quad (3)$$

This least-squares minimization problem has the solution

$$\gamma = \frac{\sum_{n=1}^N \frac{\Delta C_n M_n}{(\sigma_{\Delta C_n})^2}}{\sum_{n=1}^N \frac{M_n^2}{(\sigma_{\Delta C_n})^2}}. \quad (4)$$

Examples of this fit are given in Figures 4 and 5.

Assuming that the centroid and transit model uncertainties are uncorrelated over time, and neglecting uncertainties in the transit model values, the uncertainty in γ is

$$\sigma_\gamma = \left(\sum_{n=1}^N \frac{M_n^2}{(\sigma_{\Delta C_n})^2} \right)^{-\frac{1}{2}}. \quad (5)$$

Only in-transit cadences contribute to the computation of γ and σ_γ because $M_n = 0$ for out-of-transit cadences. Because M_n is fit to the whitened and normalized flux light curve, it has unit variance, so γ is in the same units as ΔC_n and directly gives an estimate of the in- vs. out-of-transit shift: $\Delta C \approx \gamma$. When the centroids shifts are in RA and Dec coordinates, all quarters of data can be simultaneously fit. From Equation (5) we see a $\sqrt{N^{\text{in}}}$ reduction in the uncertainty, where N^{in} is the total number of in-transit cadences, so combining many quarters increases the precision of the estimate of ΔC in each coordinate.

Once the shift is estimated in RA and Dec (in seconds of arc), the shift distance is simply

$$D = \sqrt{\Delta C_{\text{RA}}^2 + \Delta C_{\text{Dec}}^2}, \quad (6)$$

with uncertainty

$$\sigma_D = \frac{\sqrt{\Delta C_{\text{RA}}^2 \sigma_{\Delta C_{\text{RA}}}^2 + \Delta C_{\text{Dec}}^2 \sigma_{\Delta C_{\text{Dec}}}^2}}{D}. \quad (7)$$

A high-level detection statistic indicating whether a detected shift is statistically significant is also computed. This statistic measures the probability that the detected shift is due to an actual signal rather than a statistical fluctuation in white noise by subtracting the residual χ^2 from the signal χ^2 . From this statistic a significance metric is constructed that is normalized to the range $[0, 1]$, where 1 means that there is no detected shift and 0 means that the shift is highly significant. This is equivalent to Equation (4) of Wu, et al. (2010), which in our notation is given by

$$l = \frac{\sum_{n=1}^N \Delta C_n M_n}{\sigma_{\Delta C} \sqrt{\sum_{n=1}^N M_n^2}}. \quad (8)$$

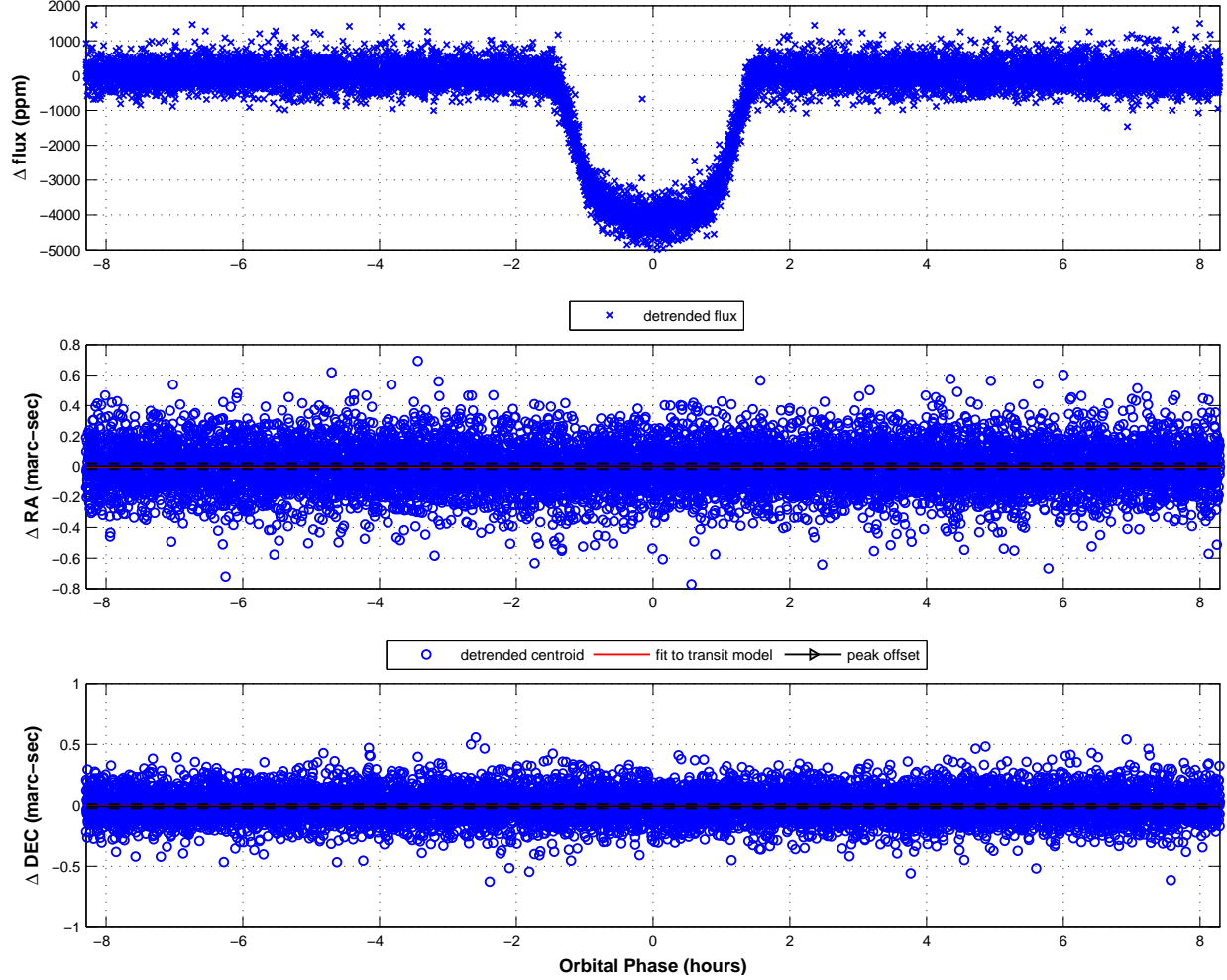


Fig. 4.— An example of a fit of the centroid time series to the transit model for a case when the transit source is at the same location as the target star (KOI-221). Top: the detrended flux light curve over all quarters folded on the transit period, with a closeup on the transit. Middle and Bottom: the RA and Dec detrended centroid shifts ΔC for the same cadences in milli-arc seconds. There is no apparent change in the centroid positions at the time of the transit.

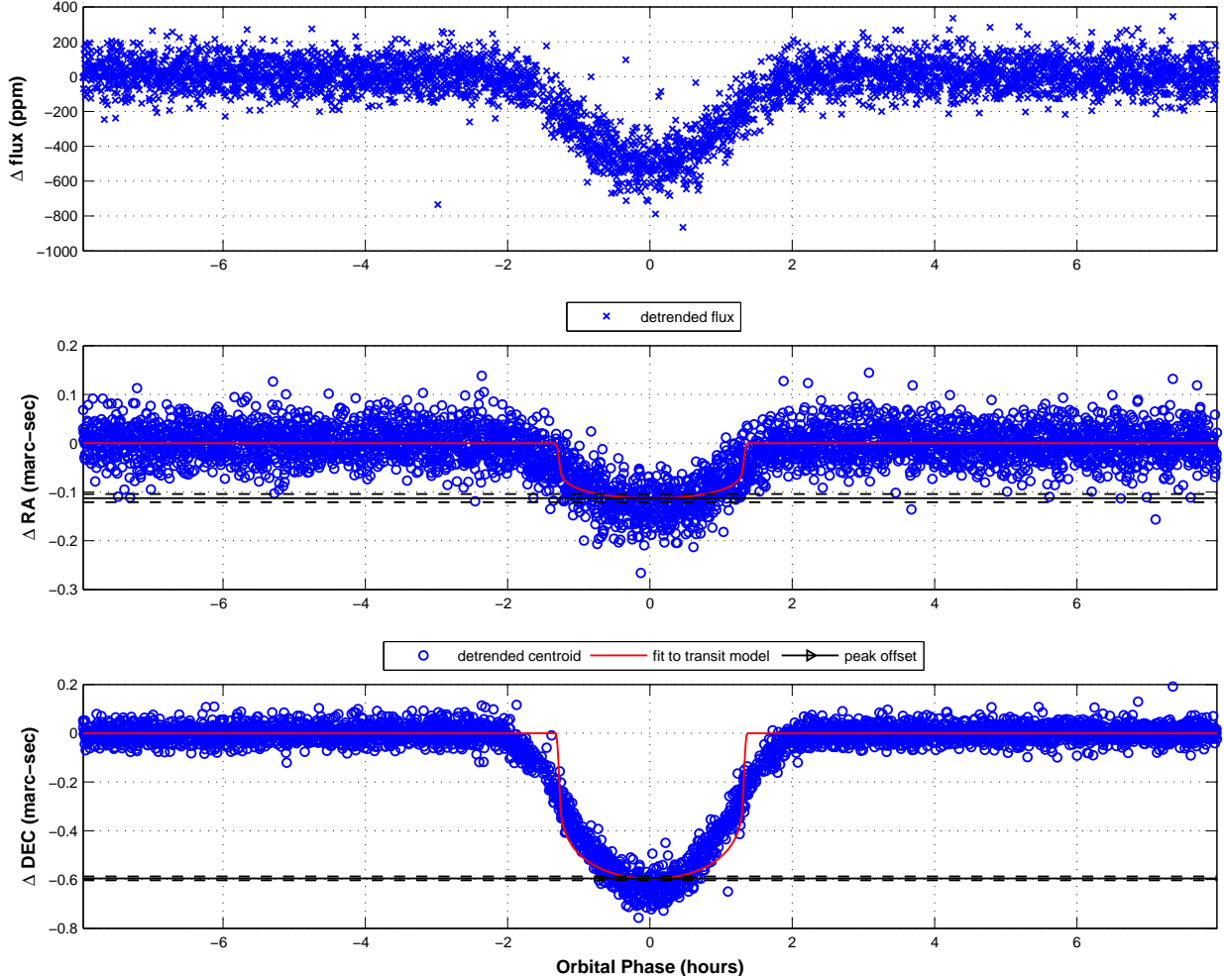


Fig. 5.— An example of a fit of the centroid time series to the transit model for a case where the transit source is offset from the target star (KOI-109). Top: the detrended flux light curve over all quarters folded on the transit period, with a closeup on the transit. Middle and Bottom: the RA and Dec centroid shifts ΔC for the same cadences in milli-arc seconds. There is a readily apparent change in the centroid shifts at the time of the transit, particularly in Dec. The transit model that best fits the flux light curve is superimposed on each centroid shift plot, scaled by the coefficient γ in Equation (4). The value of $\Delta C = \gamma$ in declination is about 0.1 milli-second of arc. The poor model fit is due to the fact that the transit source for KOI-109 is in fact a deep eclipsing binary while the model assumes a planetary transit.

2.2.1. *The impact of crowding and variability on the centroid shift estimate*

The computation of the in-transit centroid shift assumes that the transiting object is the only source of time varying flux that is correlated with the transit signal in the target star’s pixels. While this is usually a reasonable assumption, it is sometimes violated, introducing systematic error into the centroid shift estimate. A dramatic example is KOI-1860, whose pixels are shown in Figure 6. In this case there is a field star that is 2.7 magnitudes brighter than the target star at the edge of the collected pixels. Examination of the pixel flux time series shows that this bright star has moderately high variability on short time scales. In addition, because this bright star is at the edge of the collected pixels and is only partially captured, there are strong variations in flux due to spacecraft pointing jitter. The effect of these variations on the centroid time series are shown in Figure 7. These variations are on a time scale that occasionally correlates with the transit signal, leading to a small spurious measured centroid shift in the fit (4). The reconstructed transit source location using this spurious shift measurement, described in §2.3, indicates a transit source separated from the target star by about 4 arcseconds. As we will see in §3.4.1, however, the PRF-fit technique provides strong evidence that the transit source is only about a third of an arcsecond from the target star.

2.3. Estimating the Transit Source Location from Centroid Motion

Photometric centroids are the weighted average of all flux in the target star’s pixels, so they do not provide direct information about the location of the target star or the transit source. In particular, as explained in §2.1, a statistically significant shift does not necessarily imply that the transit source is offset from the target star. In Appendix A we derive a formula approximating the location of the transit source from the observed transit depth (based on the light curve created by summing the pixels used for centroiding), the out-of-transit centroid location C and the centroid shift ΔC . Remarkably, this formula applies in the presence an arbitrary background signal, including any number of field stars in or near the aperture, and does not depend on the brightness of those stars. This formula only assumes that the flux from the transit source is the only time-varying signal in the aperture, so no other stars or the background flux vary in brightness. These assumptions are never exactly true, but in many cases they are very nearly true and in these cases we can estimate the transit source location. We can then compare the transit source location to the catalog location of the target star to estimate the offset of the transit source from the target star. We assume that the centroids are provided in RA and Dec coordinates, denoted (α, δ) .

We denote the RA and Dec components of the average out-of-transit centroid as $(C_\alpha^{\text{out}}, C_\delta^{\text{out}})$,

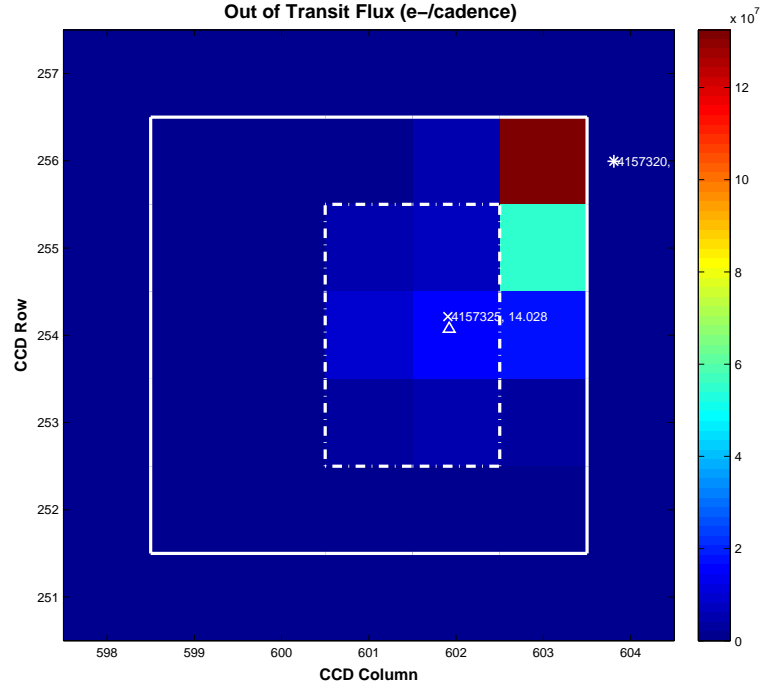


Fig. 6.— The pixels collected for KOI-1860 in quarter 10. The pixels are dominated by the field star KIC 4157320 which is 2.7 magnitudes brighter than the target star. KIC 4157320 has strong variability. In addition, because it is only partially captured in the pixels, spacecraft pointing variations are apparent in the pixel flux light curves.

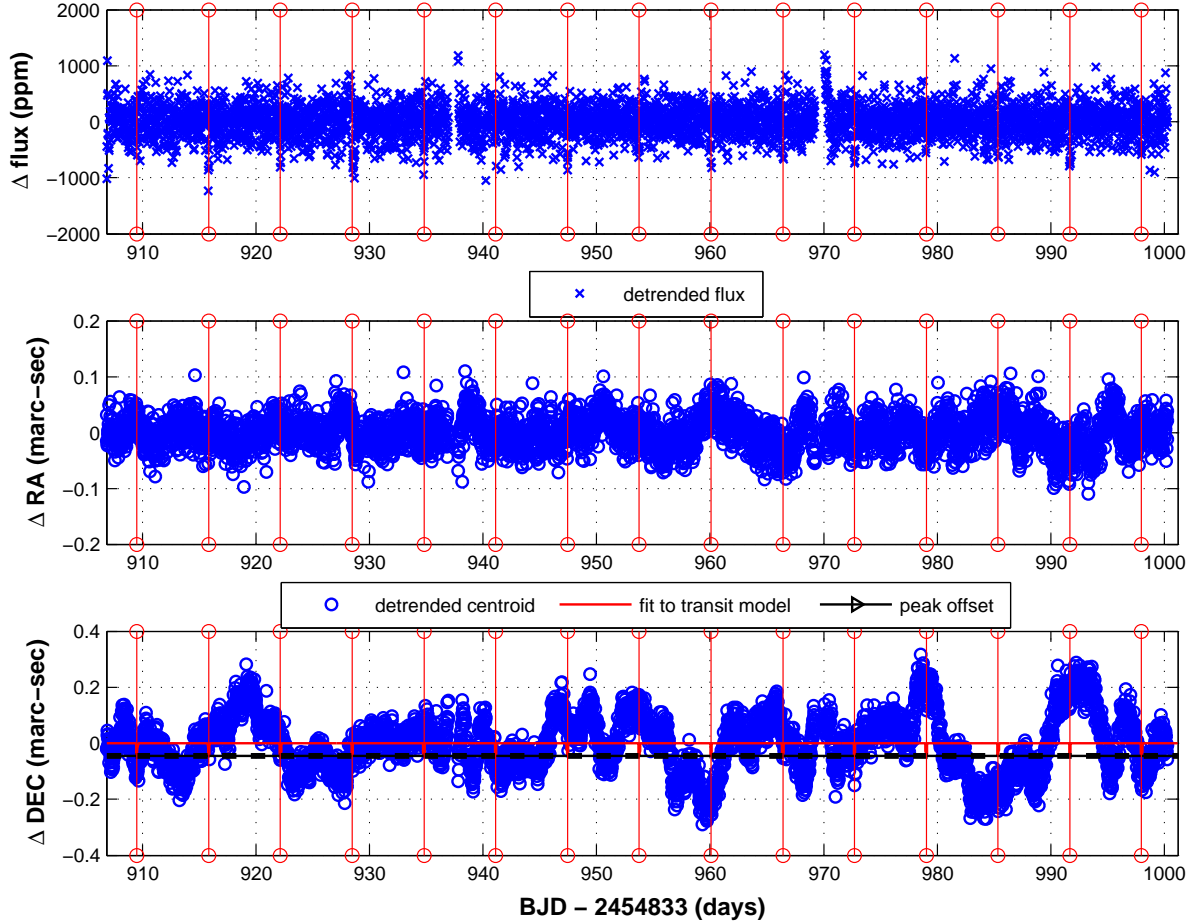


Fig. 7.— The (not folded) flux and photometric centroid time series for KOI-1860 in quarter 10. The vertical red lines indicate times of transit. The bright field star at the edge of the aperture (see Figure 6) causes strong variations in the centroid time series due to the intrinsic variability of that star combined with spacecraft pointing jitter, which is exacerbated by that star being only partially captured in the pixels. These variations cause a spurious centroid shift that is correlated with the transit signal.

and the centroid shift measured as described in §2.2 as $(\Delta C_\alpha, \Delta C_\delta)$. If the observed transit depth is d_{obs} , then as shown in Appendix A the centroid of the flux from the transit source that falls in the aperture is at RA and Dec

$$\alpha_{\text{transit}} = C_\alpha^{\text{out}} - \left(\frac{1}{d_{\text{obs}}} - 1 \right) \frac{\Delta C_\alpha}{\cos \delta}, \quad \delta_{\text{transit}} = C_\delta^{\text{out}} - \left(\frac{1}{d_{\text{obs}}} - 1 \right) \Delta C_\delta \quad (9)$$

(see Figure 8). When all flux from the transit source is captured in the aperture, then this centroid gives the location of the transit source.

The formal uncertainty in the source position is given in terms of the centroid uncertainty σ_{C_α} and depth uncertainty $\sigma_{d_{\text{obs}}}$ by

$$\sigma_{\alpha_{\text{transit}}} = \sqrt{\sigma_{C_\alpha}^2 + \left(\frac{1}{d_{\text{obs}}} - 1 \right)^2 \frac{\sigma_{C_\alpha^{\text{out}}}^2 + \sigma_{C_\alpha^{\text{in}}}^2}{\cos^2 \delta} + \frac{\Delta C_\alpha^2 \sigma_{d_{\text{obs}}}^2}{\cos^2 \delta d_{\text{obs}}^4}} \quad (10)$$

$$\sigma_{\delta_{\text{transit}}} = \sqrt{\sigma_{C_\delta}^2 + \left(\frac{1}{d_{\text{obs}}} - 1 \right)^2 (\sigma_{C_\delta^{\text{out}}}^2 + \sigma_{C_\delta^{\text{in}}}^2) + \Delta C_\delta^2 \frac{\sigma_{d_{\text{obs}}}^2}{d_{\text{obs}}^4}}. \quad (11)$$

These uncertainties do not account for systematic error due to other sources of varying flux.

For $d_{\text{obs}} \ll 1$ Equation (9) reduces to

$$\alpha_{\text{transit}} \simeq C_\alpha - \frac{\Delta C_\alpha}{d_{\text{obs}} \cos \delta}, \quad \delta_{\text{transit}} \simeq C_\delta - \frac{\Delta C_\delta}{d_{\text{obs}}}, \quad (12)$$

the approximation given in Equation (2) of Wu, et al. (2010). The uncertainties are similarly approximated by replacing $(1/d_{\text{obs}} - 1)$ by $1/d_{\text{obs}}$. This approximation has an error that is proportional to d_{obs} , which is very small for most *Kepler* planetary candidates.

Once we have the centroid source location from Equation (9), we compare it with the target location to determine the source offset. The target star location cannot, however, be reliably determined from the centroid time series, so we take the target star position from the Kepler Input Catalog. This choice potentially introduces new sources of systematic error, particularly due to unknown proper motion.

Given the target star’s catalog location $(\alpha_{\text{target}}, \delta_{\text{target}})$, we can compute the target offset and uncertainty from the offset components $\Delta\alpha = (\alpha_{\text{transit}} - \alpha_{\text{target}}) \cos \delta$ and $\Delta\delta = \delta_{\text{transit}} - \delta_{\text{target}}$ as

$$D = \sqrt{\Delta\alpha^2 + \Delta\delta^2}, \quad \sigma_D = \frac{\sqrt{\Delta\alpha^2 \sigma_{\Delta\alpha}^2 + \Delta\delta^2 \sigma_{\Delta\delta}^2}}{D} \quad (13)$$

where $\sigma_{\Delta\alpha} = \sqrt{\sigma_{\alpha_{\text{transit}}}^2 + \sigma_{\alpha_{\text{target}}}^2} \cos \delta$ and $\sigma_{\Delta\delta} = \sqrt{\sigma_{\delta_{\text{transit}}}^2 + \sigma_{\delta_{\text{target}}}^2}$.

We can now determine if the transit source is statistically significantly offset from the target star by observing whether $D > 3\sigma_D$.

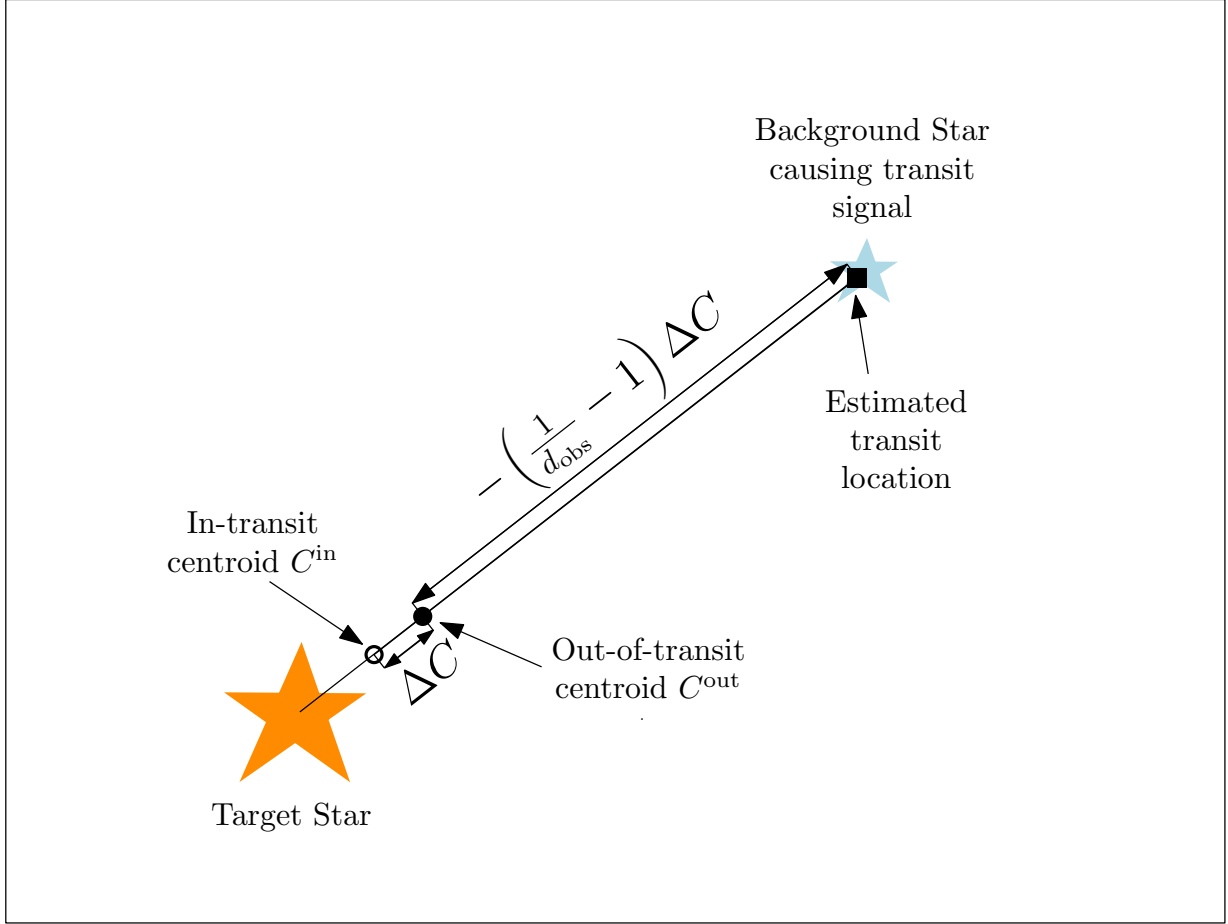


Fig. 8.— An illustration of the relationship between centroids, centroid shifts, the background eclipsing binary causing the transit signal, and the target star in Equation (9) for an otherwise empty aperture. The photometric centroid when a transit is not occurring is given by C^{out} (filled circle). If the transit is due to an eclipse on the background star, during the eclipse the centroid will shift towards the target star to C^{in} (open circle). The resulting transit shift is $\Delta C = C^{\text{in}} - C^{\text{out}}$. Applying Equation (9) gives an estimate of the transit source location (filled square), which in an idealized case will correspond to the location of the transit source.

2.3.1. Systematic errors in the source position estimate

As discussed in Appendix A, the above analysis does not describe the current implementation in the *Kepler* pipeline. The *Kepler* pipeline uses the photometrically optimal aperture (Bryson, et al. 2010) to compute the transit depth and the optimal aperture plus one ring of surrounding pixels to compute the centroid (see Figure 9). This use of different pixel apertures to compute the depth and centroid invalidates the above analysis when significant flux from the transit source falls outside the optimal aperture. Because optimal apertures are as small as a single pixel, such overshoot is possible when the transit source and target star are separated by more than one *Kepler* pixel (3.98 arcseconds).

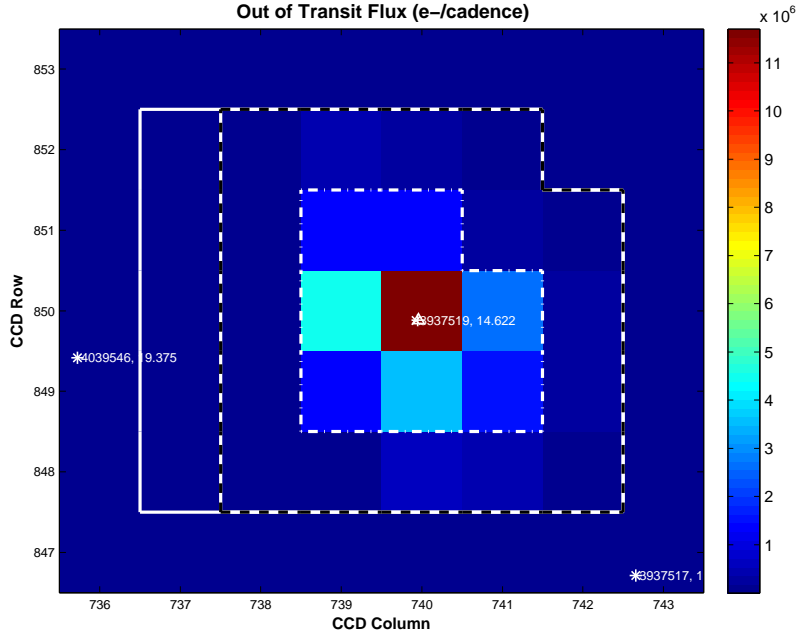


Fig. 9.— The optimal aperture compared with the pixels used for photometric centroiding. The optimal aperture pixels are outlined by the dot-dashed line, while the pixels used for photometric centroiding are outlined by the dashed line.

In the typical background false positive case when the transit source is associated with a field star that is significantly dimmer than the target star, the observed depth in the optimal aperture (the depth computed by the *Kepler* pipeline) will be smaller than the depth that would have been observed using the centroided pixels. This will result in an overestimate of the distance of the transit source from the out-of-transit photometric centroid C^{out} in Equation (9). Occasionally the field star associated with the transit source will be brighter than the target star so the flux from the target star dominates the centroids. In this case

the observed depth in both apertures will be similar, resulting in less of an overshoot. This behavior is observed in §6.1. See Appendix A for details.

The dependence of the source offset estimate on the ratio of the brightness of the background star to that of the target star is shown in Figure 10. This example is similar to that in Figure 6, where the background star causing the transit signal is outside the optimal aperture and mostly, but not completely, captured in the centroided pixels. When the background star is dim, the estimated transit source overshoots the correct offset. When the background star is significantly brighter than the target star then the flux from the background star dominates the depth estimate, so the depth based on the centroided pixels is about the same as the depth based on the optimal apertures. But because the background star is close to the edge of the centroided pixels not all flux from the background star is captured. Therefore the source offset estimate in Equation (9) gives the centroid of the flux in the pixels from the background star, which is closer to the target star than the background star itself.

3. Difference Imaging

3.1. The Concept of Difference Imaging

The difference image technique is based on the insight that subtracting the in-transit pixel values from the out-of-transit pixel values give an image that shows only those pixels that have changed during the transits. Further, if the changes during transits are due to a change in brightness of a star (as is the case for a planetary transit or an eclipsing binary) then the bright pixels in the difference image will be those of that star with flux given by the fractional transit depth times the flux of that star.

More precisely, consider a set of pixels that contain flux from M stars, labeled by the index j , at locations (α_j, δ_j) with flux b_j (we neglect background flux in this simple analysis). The PSF will distribute the flux from each of these stars over several pixels. We express the flux on the pixel at row r and column c due to star j by the unit flux function $f(\alpha_j, \delta_j, r, c)$ (so the sum over all pixels of $f(\alpha_j, \delta_j, r, c) = 1$). Then the out-of-transit pixel values due to all stars will be given by $F^{\text{out}}(r, c) = \sum_{j=1}^M b_j f(\alpha_j, \delta_j, r, c)$. If star k has a transit of depth d_{back} then during mid transit the pixel values would be given by $F^{\text{in}}(r, c) = \sum_{j=1, j \neq k}^M b_j f(\alpha_j, \delta_j, r, c) + (1 - d_{\text{back}}) b_k f(\alpha_k, \delta_k, r, c)$. In the ideal case where the only flux change is in star k , the difference image will be $F^{\text{out}}(r, c) - F^{\text{in}}(r, c) = d_{\text{back}} b_k f(\alpha_k, \delta_k, r, c)$, which is exactly the image of star k with flux $d_{\text{back}} b_k$.

Difference images provide direct information about the location of the transit source, as

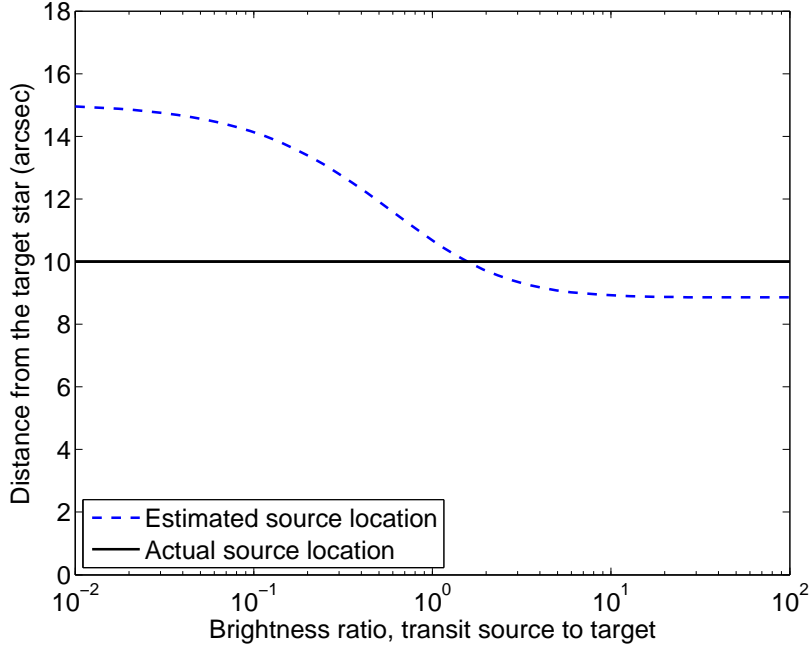


Fig. 10.— The photometric-based transit source offset as a function of the ratio of the background source brightness to the target star brightness. The example shown here is for a 0.1% transit on a background star that is 10 arcseconds from the target star. The optimal aperture in this case is 2×2 *Kepler* pixels (7.96×7.96 arcseconds), so the background star is outside the optimal aperture in the halo pixels. Because significant flux from the background star falls outside the captured pixels, the source position estimate (Equation (9)) underestimates the actual position of the background star.

opposed to the use of photometric centroids in §2.1, where the source location is inferred.

Example pixel images are shown in Figures 11 and 12. In Figure 11 we see an example of a star (KOI-221) for which there is no apparent offset between the target star and the transit source. In this case the difference image looks much like the in- and out-of-transit images, likely because the target star is itself the source of the transit (and there are no other stars of comparable brightness in the out-of-transit image). Therefore the only difference between the difference image and the out-of-transit image is the flux level in the pixels. Figure 12 shows a case (KOI-109) where the difference image is dramatically different from the out-of-transit image, and appears as a star image coincident with the dim unclassified star KIC 4752452. Because KIC 4752452 is unclassified, it does not have a *Kepler* magnitude. In this case the pixel data show that the transit source is clearly not on the target star.

When the transit SNR is high the pixel images appear as in Figures 11 (SNR = 378) and 12 (SNR = 101), with very well defined star-like difference images. When the SNR is high and the transit is on the target star, as in Figure 11, we expect the difference image to look like the out-of-transit image. Figure 13 shows an example of a low SNR transit on KOI-2949 with an SNR of 11. In this figure the difference image looks significantly different from the out-of-transit image, so a cursory inspection of only this quarter’s out-of-transit and difference images would indicate a significant offset. But examination of other quarters finds offsets in other directions in some quarters and much smaller offsets in other quarters. When the SNR is low, the difference image is subject to pixel-level systematics that can pollute the difference image. As we will see in §3.4, combining quarters puts the transit source statistically close to the target. When the SNR is very low, the difference image is dominated by noise because the transit does not have sufficient signal in individual quarters.

When the offset is as dramatic as that in Figure 12, cursory visual inspection is sufficient to determine that the transit signal does not occur on the target star. We are interested, however, in measuring smaller offsets that may not be so visually obvious. In addition we wish to have the ability to automatically measure and detect such transit-source offsets for thousands of transit signals. This can be done by measuring the centroid of the difference image and comparing with estimates of the target star position. This approach encounters several difficulties:

- Difference images can be noisy, particularly for low SNR transits. This is particularly a problem for transits near spacecraft thermal events and in multiple planet systems, where the transit signals from multiple planets can interfere with each other.
- Determination of the location of the target star should use the same method as the difference image to minimize the impact of systematic measurement errors.

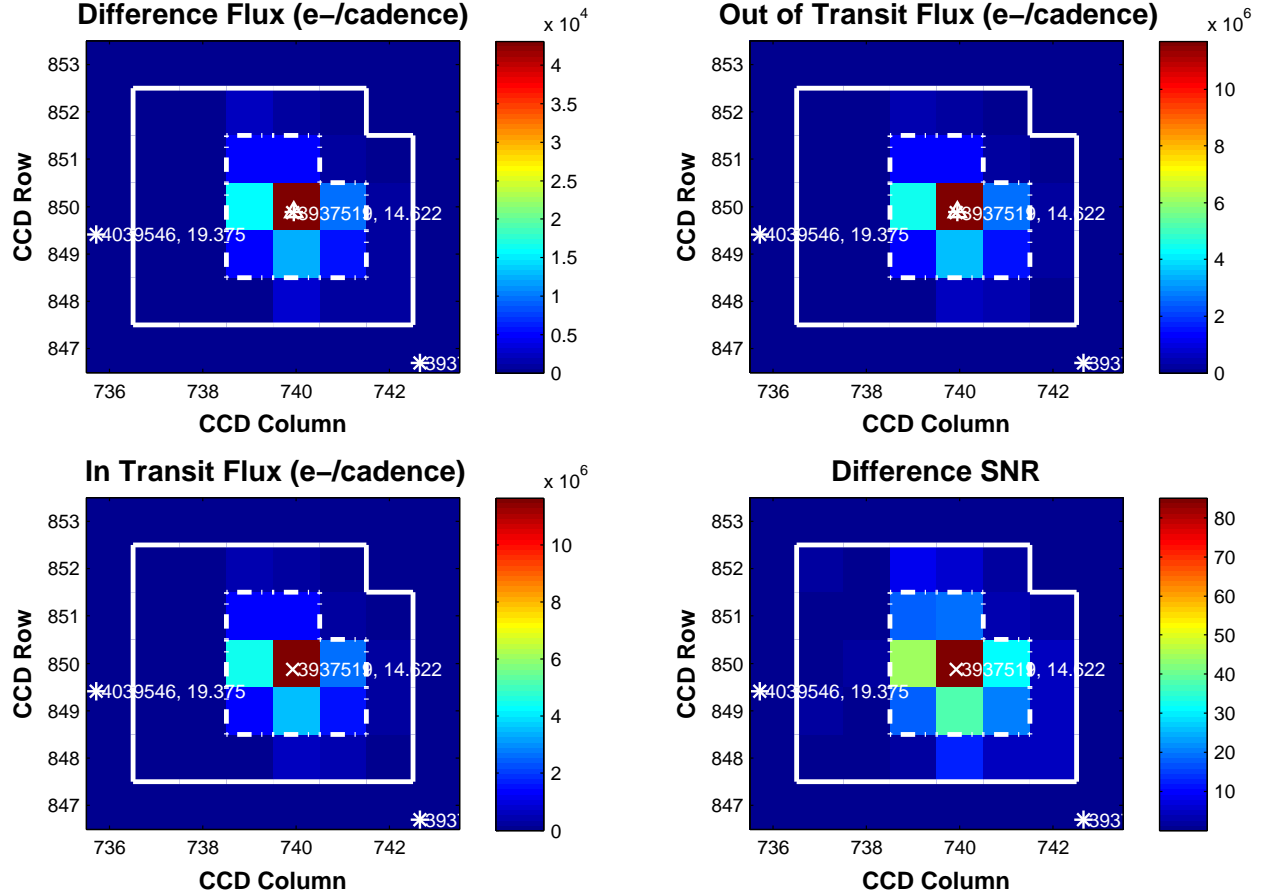


Fig. 11.— Example pixel images for KOI-221 in quarter 7, which shows no indication that the transit is not on the target star. In all figures, the dotted white line borders the pixels of the optimal aperture, while the solid white line borders all pixels collected for this target. Known stars are shown as white asterisks, with each star’s KIC catalog number and *Kepler* magnitude. Upper Right: the averaged out-of-transit pixel image. Lower Left: the in-transit pixel image. Upper Left: the difference image = out-of-transit pixel image - in-transit pixel image. Lower right: the difference image normalized by pixel value uncertainty. In this case the difference image appears identical to the in- and out-of-transit images, which indicates that the transit source is coincident with the target star.

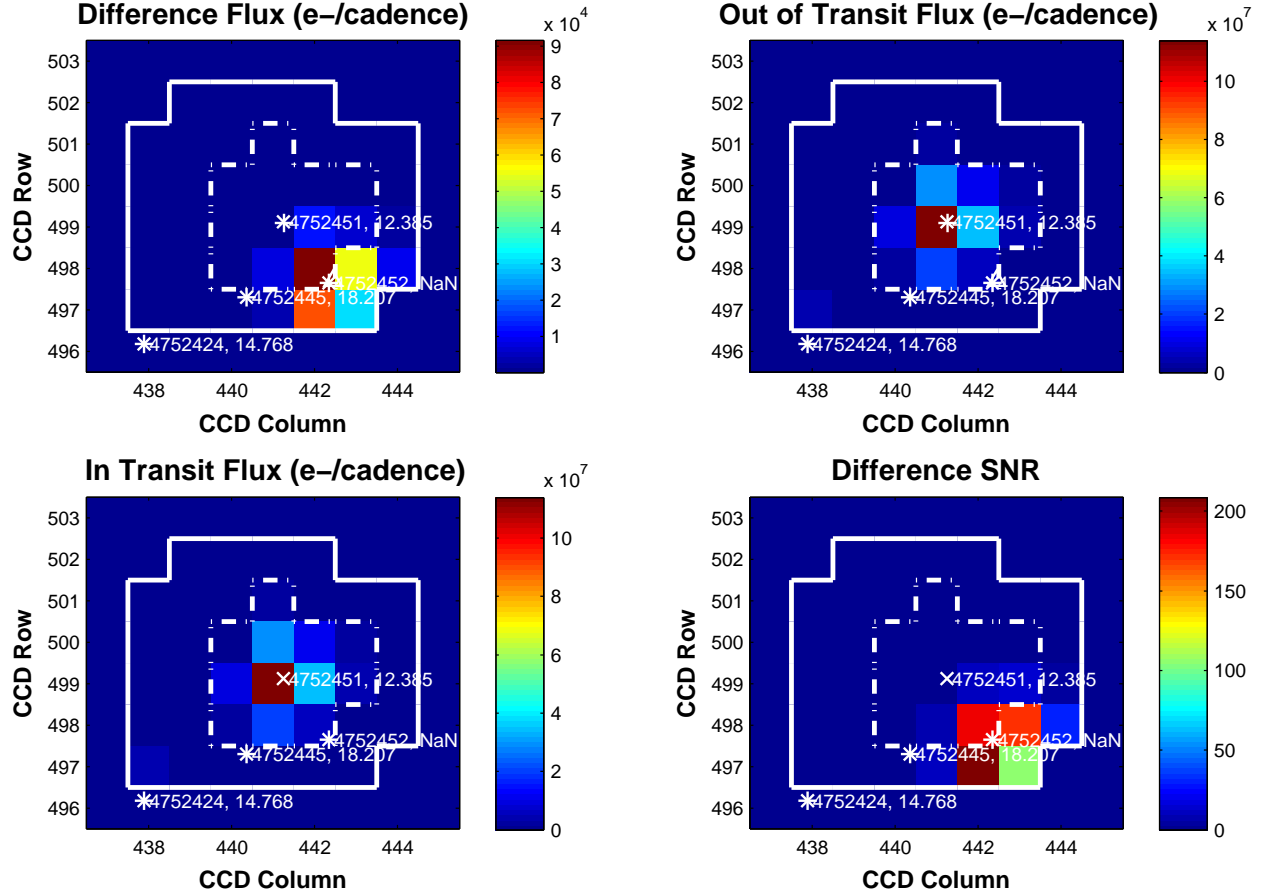


Fig. 12.— Example pixel images for KOI-109 in quarter 4, which shows indications that the transit is not on the target star. Upper Right: the averaged out-of-transit pixel image. Lower Left: the in-transit pixel image. Upper Left: the difference image = out-of-transit pixel image - in-transit pixel image. Lower right: the difference image normalized by pixel value uncertainty. In this case the difference image appears to be very different from the in- and out-of-transit images, which indicates that the transit source is coincident with the star KIC 4752452.

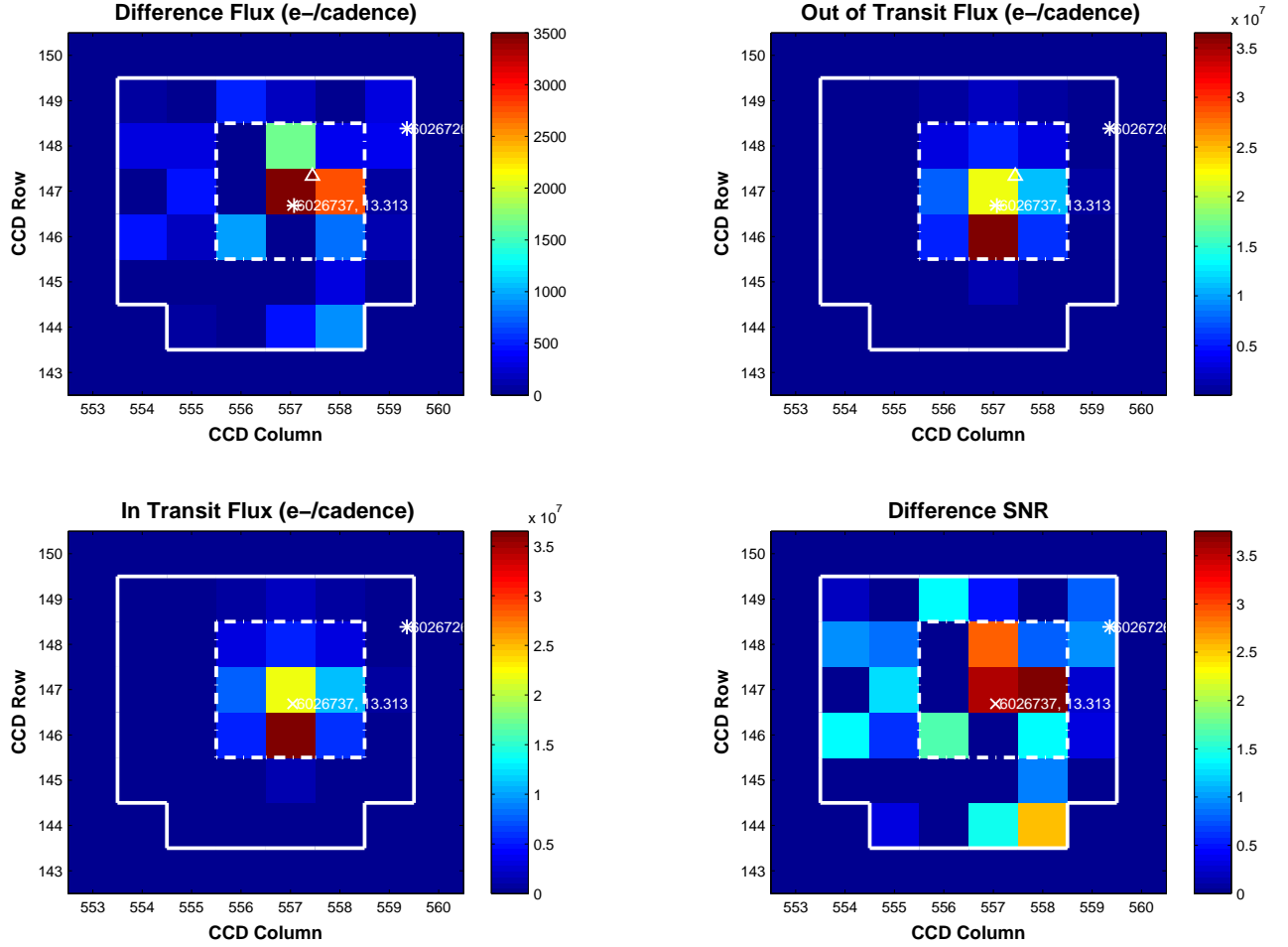


Fig. 13.— Pixel images for a low SNR transit on KOI-2949 with an SNR of 11. The difference image appears significantly different from the out-of-transit image in this quarter, indicating that the transit source is not on the target star. But other quarters show the transit source in other locations including on the target star. This situation is typical for low SNR transits, and more reliable measurement of the transit source location can be attained by combining the quarters as described in §3.4. In this example the combined quarter result indicates that the transit location is statistically consistent with the target star.

- The structure of the background signal for the target star due to crowding will be very different from the difference image background signal because non-variable background stars will cancel out in the difference image.
- In different quarters stars fall in different places on different pixels and pixel apertures vary from quarter to quarter. Therefore the offsets measured in different quarters can be different.

We address these difficulties through the following strategies:

- Careful construction of the in- and out-of-transit images, described in §3.2, so the difference image is as clean as possible.
- Determining the location of stars in the difference or out-of-transit image via PSF-type fitting to the pixel data using the *Kepler* Pixel Response Function (PRF), described in §3.3, which is more robust against noise than photometric centroids.
- Either carefully averaging the quarterly offsets (§3.4.1), or performing a joint multi-quarter fit (§3.4.2).

3.2. Construction of in- and out-of-transit and difference pixel images

Our goal is to measure the location of the change in the flux due to the transit signal. Therefore we want to create a difference image by subtracting pixel flux in transit from pixel flux near transit. We want to avoid pixel flux away from the transit so changes due to stellar variability are less likely to enter into the difference image. We also want to avoid changes in flux that are not related to the transit under examination, such as spacecraft thermal or pointing events or transits due to other planets orbiting the target star in multiple systems. We minimize noise by averaging as many in- and out-of-transit measurements as possible subject to these constraints.

In each quarter, *Kepler* collects about 4300 long cadences, from which in- and out-of-transit exposures need to be identified. We use the (unwhitened) transit model M_n constructed in Data Validation (Wu, et al. 2010) to select these cadences.

In-transit cadences are defined as those cadences where the model is less than a threshold proportional to the model transit depth. The current threshold is $3/4$ of the transit depth: when the model is normalized so that $M_n = 0$ for out-of-transit cadences, in-transit cadences are those for which the model values $M_n < -\frac{3}{4}d$, where d is the modeled fractional transit depth.

The out-of-transit cadences are chosen near each transit under the following criteria:

- Out-of-transit cadences are chosen on both sides of the transit so that an average of these out-of-transit cadences removes any locally linear secular trends.
- Not too many cadences are chosen so that nonlinear variability on time scales longer than the transit are small.
- Out-of-transit cadences should not be too close to the transit.

The number of out-of-transit cadences N_{out} is chosen as the number of cadences that occur during the entire transit duration where $M_n < 0$. This is generally not the same as N_{in} . The out-of-transit cadences are chosen to lie more than N_{buffer} cadences from the cadences for which $M_n < 0$. Fig. 14 shows an example of selected cadences for a typical transit.

After in- and out-of-transit cadences are chosen they are excluded if they are associated with any of the following events:

- Data gaps such as Earth points and safe modes.
- Cadences within a day after major spacecraft thermal events, such as recovery from Earth points and safe modes that significantly change the temperature distribution of the spacecraft and require many hours to return to thermal equilibrium.
- Pointing anomalies such as attitude tweaks, and loss of fine-point events.
- Interference by transits from other planets in multiple planet systems. An example of such interference is shown in Figure 15

If more than a small number of cadences associated with a transit are excluded then the entire transit is excluded from the construction of the difference image. This threshold is currently set to zero, so if any cadences are excluded then the entire transit is excluded. As *Kepler* detects longer-period transits, so fewer transits will be available, this threshold will be relaxed to one or two excluded cadences per transit.

Once the final set of transits and their in- and out-of-transit cadences are identified, the in-transit pixel values are averaged to produce the in-transit image and the out-of-transit cadences are averaged to produce the out-of-transit image. The pixel values are not whitened or otherwise detrended: we rely on the averaging described in this section to remove local secular trends. First the average pixel values are computed for each transit, then each

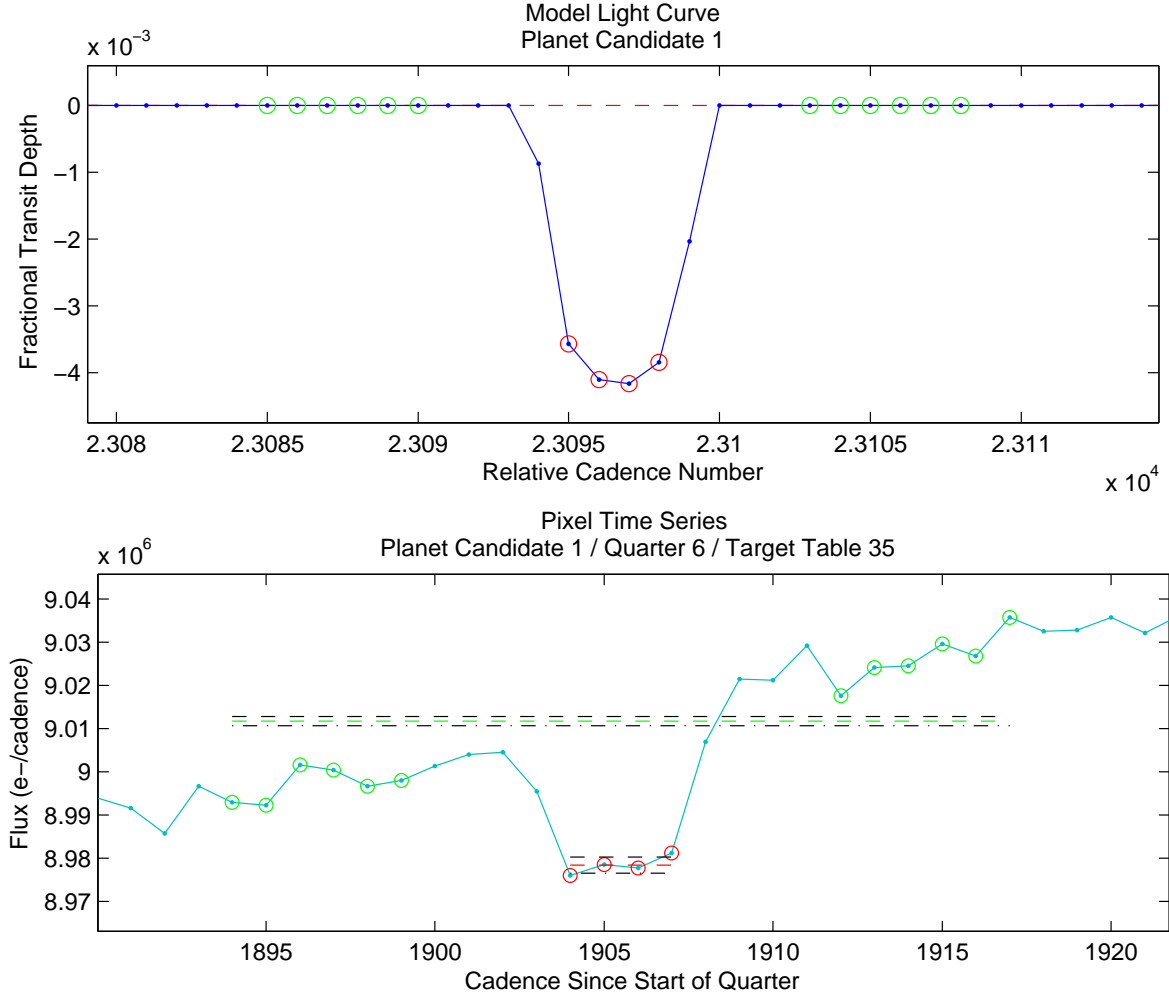


Fig. 14.— An example of in- and out-of-transit cadence selection (KOI-221). Top: the transit model M_n for a selected cadence range in quarter 6. The x -axis shows the cadences since the beginning of the *Kepler* science operations. The circles at the bottom of the transit show the cadences that were chosen for the in-transit image. $N_{\text{in}} = 4$ cadences were chosen in the transit because they are below the threshold described in the text. The circles outside the transit show the cadences chosen for the out-of-transit image. The full transit is six cadences wide so $N_{\text{out}} = 6$ cadences were chosen on both sides of the transit. The out-of-transit cadences are $N_{\text{buffer}} = 3$ cadences from the transit. Bottom: the actual transit in one of the brighter pixels. The x -axis shows the cadences since the beginning of quarter 6.

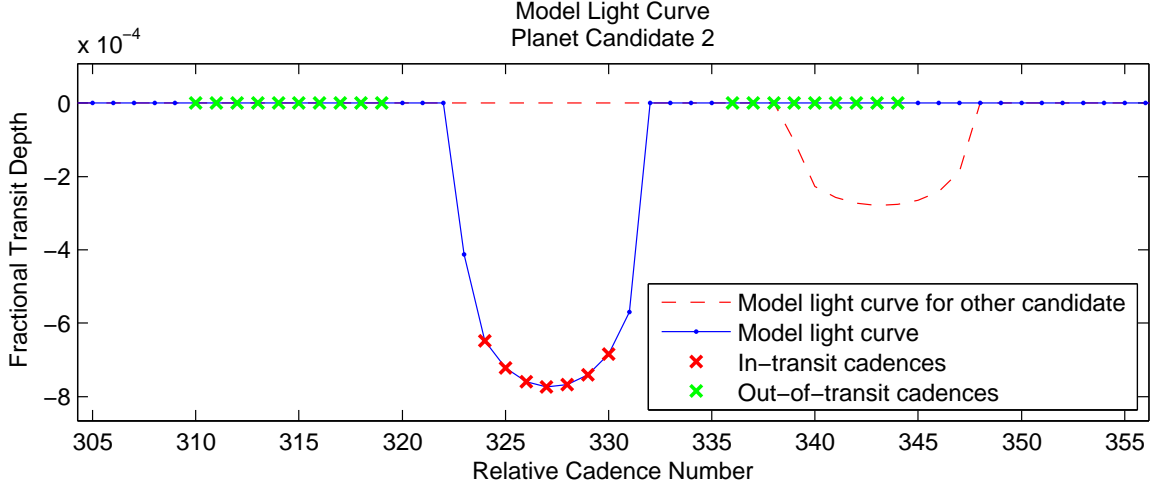


Fig. 15.— An example of the interference with cadences chosen for a transit in the Kepler-11 system. Seven out-of-transit points to the right of the transit are excluded because of the interfering transit by the other planet candidate, which causes the entire transit to be excluded from the construction of the average pixel images.

transit’s averaged pixels in a quarter are averaged together to produce the final in- and out-of-transit average pixel images for that quarter. The difference image for the quarter is then the out-of-transit pixel image minus the in-transit pixel image.

3.3. Fitting the Pixel Response Function

In this section we describe how the *Kepler* pixel response function (PRF) (Bryson, et al. 2010) is used to provide a robust, high-precision estimate of the target star and transit locations using the average out-of-transit and difference images constructed as described in §3.2. This technique requires that the target star is several magnitudes brighter than other stars in the out-of-transit pixels, and that the transit signal is sufficiently strong in the difference image. In §3.3.2 we describe a quantitative measure of whether the average images for a given target star have the required properties. §3.3.1 describes various ways in which this method can be compromised and discuss mitigation strategies.

The PRF gives the long-cadence brightness of a pixel due to a star at a specified location. The PRF can be thought of as the convolution of the optical PSF with the effects of pointing, sub-pixel response and system electronics. In this section we write the PRF as a unit flux function $f(\alpha, \delta, r_i, c_i)$ so $\sum_{i=1}^{P_{\text{total}}} f(\alpha, \delta, r_i, c_i) = 1$, where P_{total} is the number of all pixels

that contain flux from a star at sky coordinates (α, δ) , and r_i and c_i are those pixels' row and column coordinates. If the star has flux b , then the value of a pixel at row r_i and column c_i due to that star will be $p_i = bf(\alpha, \delta, r_i, c_i)$, and the sum of all pixels containing flux from that star is $\sum_{i=1}^{P_{\text{total}}} p_{r_i, c_i} = b$. (In Bryson, et al. (2010) the star location is defined in pixel coordinates rather than sky coordinates. In this paper we include the projection from sky coordinates to pixel coordinates in the PRF function f).

Assume we are given a set of P pixel values p_i with rows r_i and columns c_i that form a pixel image. The P pixels need not contain all the flux from the target star, so P may be less than P_{total} . A PRF fit to these pixels is the determination of sky coordinates $(\alpha_{\text{fit}}, \delta_{\text{fit}})$ and flux b_{fit} that minimize the function

$$\chi^2 = \sum_{i=1}^P \frac{1}{\sigma_{p_i}^2} (p_i - bf(\alpha, \delta, r_i, c_i))^2 \quad (14)$$

where σ_{p_i} is the uncertainty in the pixel value p_i . This fit is performed iteratively via the non-linear Levenberg-Marquardt algorithm (Levenberg 1944; Marquardt 1963). Formally this is a three dimensional fitting problem in the parameters α , δ and b . The fit to b , however, can be reduced to a linear problem once the position is known, so this problem can be treated as a much faster two-dimensional non-linear fit in α and δ . In each iteration of the Levenberg-Marquardt algorithm the pixels p_i at (r_i, c_i) and the fit parameters α and δ are provided to the model function. We first evaluate the uncertainty-normalized *Kepler* PRF at α and δ , computing $\hat{p}_i = f(\alpha, \delta, r_i, c_i) / \sigma_i$ for each pixel. The flux b is the linear least-squares fit of the input pixel values p_i to the model $b\hat{p}_i$, given by

$$b = \frac{\sum_{i=1}^P p_i \hat{p}_i}{\sum_{i=1}^P \hat{p}_i^2}. \quad (15)$$

The product $b\hat{p}_i$ is then returned by the model function. The Levenberg-Marquardt algorithm seeks the α and δ that minimizes $\sum_{i=1}^P (p_i - b\hat{p}_i / \sigma_i)^2$ after several iterations. (In the *Kepler* pipeline this is implemented as a model function passed to the MATLAB function *nlinfit*.) Once the iteration has converged, providing $(\alpha_{\text{fit}}, \delta_{\text{fit}})$, the final estimate of b can be computed as $b_{\text{fit}} = \left(\sum_{i=1}^P p_i \hat{p}_i \right) / \left(\sum_{i=1}^P \hat{p}_i^2 \right)$, where now $\hat{p}_i = f(\alpha_{\text{fit}}, \delta_{\text{fit}}, r_i, c_i) / \sigma_i$.

The typical implementation of the Levenberg-Marquardt algorithm returns the Jacobian J , which contains the derivatives of the model function with respect to position. To estimate the uncertainty of the fit location we need the Jacobian of the position with respect to the pixel values given by the model function. We obtain this by inverting J , using the pseudo-inverse, to give the transformation $T = (J^T J)^{-1} J^T$. T is a $P \times 2$ matrix, and the columns of T are normalized by the pixel uncertainties: $T_{ij} \rightarrow T_{ij} / \sigma_i$ for $j = 1, 2$. Then the PRF fit

location covariance matrix is $\mathcal{C} = T^T \mathcal{C}_{\text{pixel}} T$, where $\mathcal{C}_{\text{pixel}}$ is the pixel covariance, and the fit location uncertainties are the square root of the diagonal of \mathcal{C} : $\sigma_\alpha = \sqrt{\mathcal{C}_{1,1}}$ and $\sigma_\delta = \sqrt{\mathcal{C}_{2,2}}$.

The PRF is fit separately to the difference image and the out-of-transit image. Because the fit to the difference image $(\alpha_{\text{diff}}, \delta_{\text{diff}})$ measures the position of the transiting source and the fit to the out-of-transit image $(\alpha_{\text{OOT}}, \delta_{\text{OOT}})$ measures the position of the target star, the offset of the transit source from the target is simply $(\Delta\alpha, \Delta\delta) = ((\alpha_{\text{diff}} - \alpha_{\text{OOT}}) \cos \delta_{\text{OOT}}, \delta_{\text{diff}} - \delta_{\text{OOT}})$. Then the offset distance and uncertainty are computed as in Equation 13.

In- and out-of-transit pixel images, and therefore difference images, can only be constructed on a quarter-by-quarter basis. Images cannot be combined across quarters in a useful way because

- The same star will fall on slightly different pixel locations in each quarter due to pointing differences and small asymmetries in the construction of the *Kepler* focal plane.
- The *Kepler* PRF at the star’s location can have large changes from quarter to quarter.
- The pixel aperture generally varies in both size and shape from quarter to quarter.

Two approaches to combining quarters will be described in §3.4.

3.3.1. Systematic PRF fit error

Systematic error in the PRF fit arises from primarily from two classes of sources: error in the PRF model being fit and crowding. These errors cause biases in the offset vector $(\Delta\alpha, \Delta\delta)$. There are various ways to control systematic PRF fit errors, so we examine these errors in detail.

Sources of PRF fit error

PRF Model Error The PRF model contains various sources of error (Bryson, et al. 2010) which lead to *a priori* unpredictable bias in the PRF-fit centroid. Because the target star falls on different parts of the *Kepler* field of view in different quarters, variation of the PRF across the focal plane causes the PRF error bias to vary from quarter to quarter.

Crowding Bias The PRF fit is a single-star fit, and therefore assumes that the target star in the out-of-transit image and the transit signal in the difference image are the only

stars present in the pixels. This is rarely the case in the out-of-transit image and sometimes not the case in the difference image due to variability of field stars. Unlike the case of photometric centroids described in §2, the effect of crowding on the PRF fit is difficult to predict. Because field stars mostly cancel in the difference image, the crowding signal in the out-of-transit and difference images can be very different. Therefore the PRF fit to the out-of-transit and difference images can have very different biases, which leads to errors in the offset vector $(\Delta\alpha, \Delta\delta)$. An example of a target with a large amount of crowding is shown in Figure 16.

In the worst case there is a field star in the out-of-transit image brighter than the target star, so the PRF fit to the out-of-transit image returns the centroid of the field star rather than the target star. When this bright field star cancels in the difference image, so the difference image is dominated by a transit on the target star, the offset vector $(\Delta\alpha, \Delta\delta)$ gives the distance of the transit signal from the field star rather than the target star. The result is an incorrect measurement of a significant offset of the transit source from the target star. An example of this situation, KOI-1860 (discussed in §2.2.1), is shown in Figure 17.

Mitigation of the impact of PRF fit error within a quarter

Average out-of-transit and difference images are computed for each quarter, and these are fit by the PRF to estimate the offset of the transit source from the target star. PRF model error and crowding contribute systematic errors in this estimate. Here we discuss ways to mitigate these systematic errors within each quarter. In §3.4.1 we discuss ways the possibility of averaging out these systematics across quarters.

The *Kepler* PRF for nearby stars will be very nearly the same, so the PRF model error for those stars will be similar. Assuming low crowding, the PRF fit of the out-of-transit image and the fit to the difference image will have similar biases due to PRF model error. When forming the offset vector $(\Delta\alpha, \Delta\delta)$ as the difference between these two fits, these biases should approximately cancel. We therefore prefer the offset vector computed as the difference between the two out-of-transit fits when the target star is not highly crowded.

When the target star is highly crowded, crowding bias will dominate the out-of-transit PRF fit but rarely the difference image PRF fit. This bias is usually due to an error in the measurement of the target star position. As an alternative we compute the transit source offset relative to the target star’s catalog position. We define $(\Delta\alpha, \Delta\delta)_{\text{catalog}} = ((\alpha_{\text{diff}} - \alpha_{\text{catalog}}) \cos \delta_{\text{catalog}}, \delta_{\text{diff}} - \delta_{\text{catalog}})$, where $(\alpha_{\text{catalog}}, \delta_{\text{catalog}})$ is the catalog position of the target star (usually from the *Kepler* input catalog). When $(\Delta\alpha, \Delta\delta)$ differs from $(\Delta\alpha, \Delta\delta)_{\text{catalog}}$ by more than a *Kepler* pixel (3.98 arcseconds), the out-of-transit measurement of the target

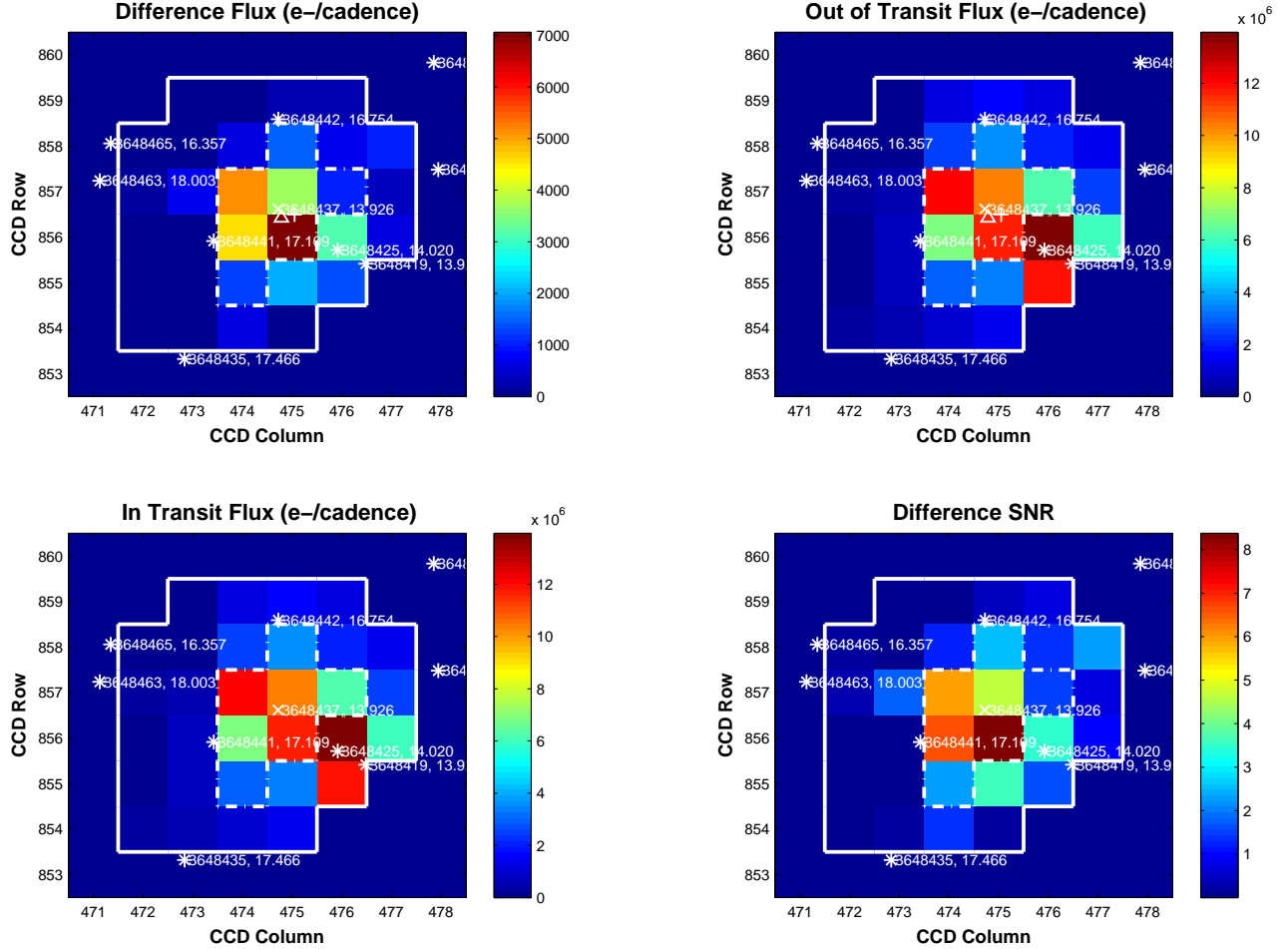


Fig. 16.— An example of a target with large amounts of crowding (KOI-1861). The in- and out-of-transit images do not appear as a typical star, and the fact that this is due to crowding is indicated by the large number of asterisks on the image indicating many relatively bright background stars. The difference image, on the other hand, looks much more like a star because most of the background stars in the image have cancelled out, though there is still some residual background contamination. In this case the fit to the out-of-transit image will have a large bias relative to the target star, while the bias in the difference image fit will be much smaller. This results in a biased offset measurement of the transit source relative to the target star. Visual inspection of the difference image, however, indicates that the transit source is closer to the target star than the biased measurement would indicate.

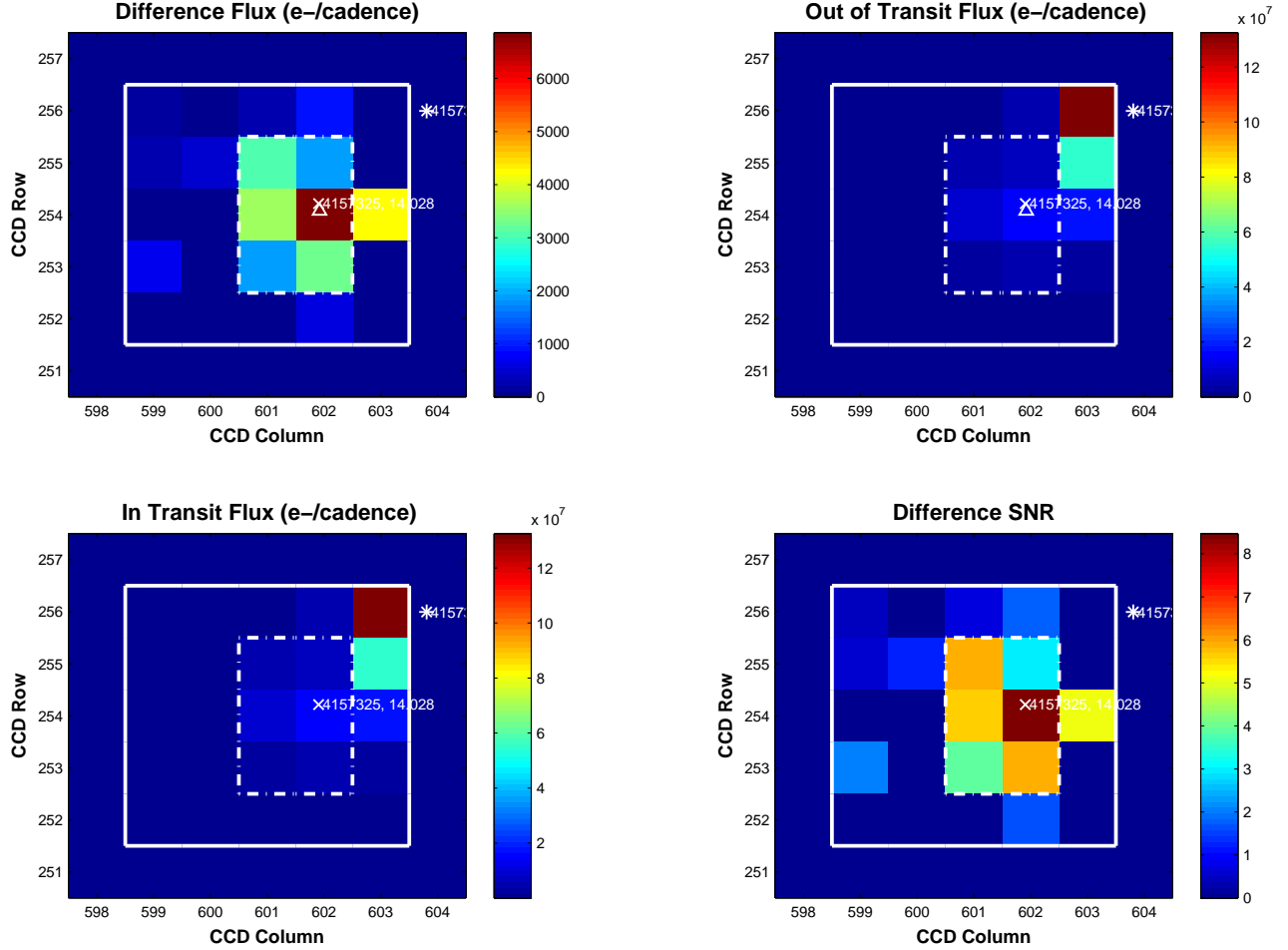


Fig. 17.— An example of a target with bright field star that captures the out-of-transit PRF fit (KOI-1860). The out-of-transit image is dominated by the bright star in the upper right corner, so this field star position will be returned by the PRF fit to the out-of-transit image. The difference image, however, shows a nicely star-shaped pattern at the location of the target star, so the target star position will be returned by the PRF fit to the difference image. The resulting offset vector measures the distance of the transit source (target star in this case) to the bright field star rather than the distance of the transit source to the target star. In this case blindly using the offset values would lead to the erroneous identification of a background false positive.

star position $(\alpha_{\text{OOT}}, \delta_{\text{OOT}})$ likely contains large errors and the offset vector $(\Delta\alpha, \Delta\delta)$ should be considered unreliable. The catalog-based offset error $(\Delta\alpha, \Delta\delta)_{\text{catalog}}$ can be used instead, but is itself subject to error because a) it does not mitigate fit error due to PRF error and b) is subject to catalog errors due to, for example, unknown proper motion of the target star. In this case the PRF fit results should be considered qualitative and to have lower accuracy than non-crowded targets, regardless of the formal propagated uncertainty. In the example in Figure 17 the magnitude of the offset vector in that quarter is about 11 arcseconds, while the magnitude of the offset from the catalog position is about 0.6 arcseconds.

A work in preparation (Bryson and Morton 2013) will describe the use of modeling to identify and mitigate bias due to crowding.

In the majority of cases the bias will be due to a mix of crowding and PRF model error, with comparably small contributions from each. In this case we reduce the overall bias by taking advantage of the variation in bias across quarters via averaging as described in §3.4.

3.3.2. PRF Fit Quality

The quarterly out-of-transit and difference images can be polluted by various types of contamination. For example the out-of-transit image may have bright stars in addition to the target star. The difference image may have more than one stellar image due to the variability of a field star, or the transit may have low SNR, causing the difference image to be poorly formed as in Figure 13. These cases will degrade the reliability of the PRF-fit source offset measurement. The quality of the PRF fit can be determined by evaluating the PRF at the fit position, creating a synthetic pixel image containing only one star at that position, and compare this to the observed average pixel image. This synthetic image will have the pixel values $\tilde{p}_i = b_{\text{fit}} f(\alpha_{\text{fit}}, \delta_{\text{fit}}, r_i, c_i) (= b_{\text{fit}} \hat{p}_i)$, where the subscript “fit” refers to “diff” or “OOT” as appropriate. These can be compared to the actual pixel values p_i to determine if the fitted PRF reproduces the observed pixels. One simple comparison is to compute the correlation between \tilde{p}_i and p_i , and declare the fit good if this correlation is above some threshold. For the difference image fit quality we set the threshold to 0.7. When the correlation is below this threshold, then the difference image is likely dominated by noise, typically because the transit has a very low SNR. When the correlation is below threshold for the out-of-transit fit, then it is likely that there is more than one bright star in the image, which compromises the fit due to crowding. In both cases the source offset measurement is likely to be unreliable.

3.4. Combining Quarterly Results

A comparison of PRF-fit star positions with their catalog RA and Dec show that the combination of crowding and PRF error bias has an approximately Gaussian distribution with a median of 1 millipixel (0.004 arcsec) and a median absolute deviation of 22 millipixels (0.09 arcsec) (Bryson, et al. 2010). While the quarter-to-quarter variation in the PRF fit of a particular star can have larger spreads, we find that for most stars this quarter-to-quarter variation is approximately zero-mean on average. We therefore combine the quarterly offsets to improve the precision of the PRF-fit centroid offset vector.

3.4.1. Multi-Quarter Averaging

We denote the single-quarter PRF fit offset vectors by $(\Delta\alpha_q, \Delta\delta_q)$, where q labels the quarter. A simple average of Q quarters, $\frac{1}{Q} \sum_{q=1}^Q (\Delta\alpha_q, \Delta\delta_q)$ with its uncertainties $\frac{1}{Q} \sqrt{\sum_{q=1}^Q (\sigma_{\Delta\alpha_q}^2, \sigma_{\Delta\delta_q}^2)}$ can be used but this has the weakness that the uncertainties do not reflect scatter in the quarterly averages. For example a set of points on a large circle with some uncertainty will have the same average and average uncertainty as a set of points with the same uncertainty that all lie at the center of the circle. We would like the uncertainty to reflect the scatter of the quarterly offsets.

We accomplish this by treating the quarterly offset vectors and their uncertainties as a time series, and compute the average offset $(\overline{\Delta\alpha}, \overline{\Delta\delta})$ by robustly fitting this time series with a constant. In other words we compute a least-squares robust fit of a 0th-order polynomial to the quarterly data, minimizing

$$\sum_{q=1}^Q \frac{1}{(\sigma_{\Delta\alpha_q})^2} (\Delta\alpha_q - \overline{\Delta\alpha})^2, \quad \sum_{q=1}^Q \frac{1}{(\sigma_{\Delta\delta_q})^2} (\Delta\delta_q - \overline{\Delta\delta})^2. \quad (16)$$

We compute a robust fit to suppress statistical outliers in the belief that these are due to transient biases resulting from systematic events such as pointing or thermal anomalies. The uncertainties in the above fit are typically returned by the robust fit algorithm used to compute $(\overline{\Delta\alpha}, \overline{\Delta\delta})$. Care must be taken when estimating these uncertainties *a priori* from the quarterly data because every fourth quarter the spacecraft orientation is strongly correlated.

The above estimate of the average uncertainty assumes Gaussian statistics. While PRF fit biases appear nearly Gaussian in the statistical sense, they may not be Gaussian for individual targets. We therefore compute an alternative uncertainty via bootstrap anal-

ysis, which provides a more general estimate of the uncertainty. We use a resample-with-replacement strategy, creating an ensemble of Q^2 simple multi-quarter averages. Specifically, given the set of Q measured offsets $(\Delta\alpha_1, \Delta\alpha_2, \dots, \Delta\alpha_Q)$, Q^2 realizations are created, where in each realization we replace each element with an offset randomly chosen from the measured set. Examples of these realizations when $Q = 5$ include $(\Delta\alpha_3, \Delta\alpha_1, \Delta\alpha_5, \Delta\alpha_4, \Delta\alpha_2)$ and $(\Delta\alpha_2, \Delta\alpha_4, \Delta\alpha_1, \Delta\alpha_4, \Delta\alpha_1)$. Averages are computed for each of these realizations, and the standard deviation of the resulting ensemble of Q^2 averages provides the bootstrap uncertainty estimate. The bootstrap uncertainty is typically very similar to the uncertainty returned by the robust fit described above, but can be significantly different for specific targets. We choose the larger of the two uncertainty estimates as the final uncertainty estimate for the multi-quarter average $\sigma_{\Delta\alpha}$. A similar analysis applies to $\sigma_{\Delta\delta}$.

Examples of this multi-quarter averaging technique are shown in Figures 18 through 22. Figure 18 shows a case with no significant offset while Figure 19 shows a case with a significant offset, indicating that the transit signal is on a background star. For long-period transiting planets, where there are few quarters that contain transits, the benefits of multi-quarter averaging will diminish. In such cases, however, multi-quarter averaging can often provide good results, an example of which is shown in Figure 20. Figure 21 shows the low SNR example discussed in §3.1, where we see that there is a large scatter in the quarterly measurements, but the multi-quarter average is within three standard deviations of the target star.

The case of KOI-1860, where a bright field star at the edge of the captured pixels introduces large systematic error, is examined in Figure 22. The offset relative to the out-of-transit centroid is measured to be about 4 arcseconds, which is a statistically significant 4σ . For most quarters, particularly those which would show a larger offset, the PRF fit to the out-of-transit image failed because the bright star falls very close to the edge of the captured pixels. The offset relative to the catalog position, however, is much smaller, with a multi-quarter average of about 0.3 arcseconds or 1σ . Because we are aware of the bright star crowding for KOI-1860, we defer to the offset relative to the catalog position, which is not statistically significant.

We demonstrate the increased precision of the multi-quarter average in Figure 23. The offset distance from the target catalog position is shown for both individual quarter PRF fits and their quarterly average. This analysis uses 2,278 KOIs whose quarterly averaged offsets are less than 3σ and whose offsets from the target are < 5 arcseconds in the Q1-Q12 data. The left panel shows the 21,401 individual quarter offsets, while the right panel shows the offset of the average over all quarters for each target. The individual quarter offsets have a standard deviation of 0.90 arcseconds, while the multi-quarter averages over 12 quarters

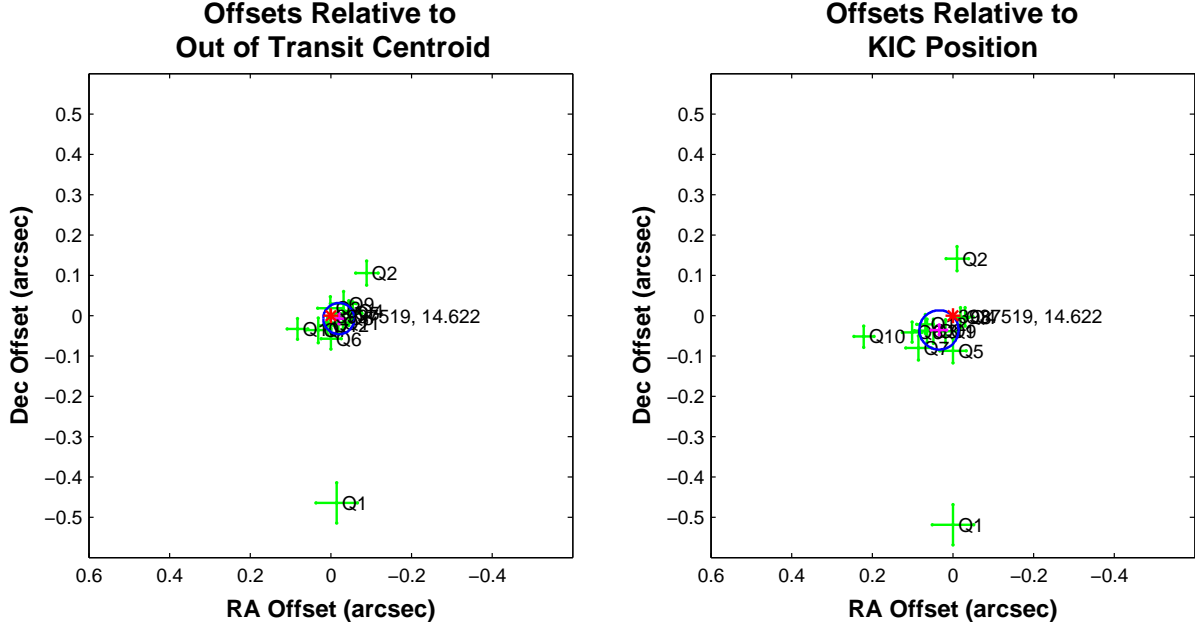


Fig. 18.— An example of multi-quarter offset analysis when the transit signal seems to be on the target star (KOI-221). In both figures the x - and y -axes give the offsets $\Delta\alpha$ and $\Delta\delta$, with $(0,0)$ being the catalog location of the target star. The green crosses show the individual quarter offsets labeled by quarter, and the length of the crosses are equal to the uncertainties $\sigma_{\Delta\alpha}$ and $\sigma_{\Delta\delta}$. The location of the multi-quarter average $(\overline{\Delta\alpha}, \overline{\Delta\delta})$ is shown as a magenta cross (obscured by the tight cluster of green crosses). The blue circle has radius equal to three times the uncertainty in the magnitude of $(\overline{\Delta\alpha}, \overline{\Delta\delta})$. Star locations relative to the target star are shown as asterisks, with the target star in red (there happen to be no other stars in this figure). The KIC catalog number and *Kepler* magnitudes are shown next to each star. We see that most offsets are tightly clustered within 0.1 arcseconds of the target star with Q1 and Q2 as outliers. Left: the offsets $(\Delta\alpha, \Delta\delta)$ relative to the PRF fit to the out-of-transit centroid. Right: the offsets $(\Delta\alpha, \Delta\delta)_{\text{catalog}}$ relative to the catalog position of the target star. The difference between the left and right plots is not a simple translation because the two plots have different biases due to PRF error and crowding (see §3.3.1).

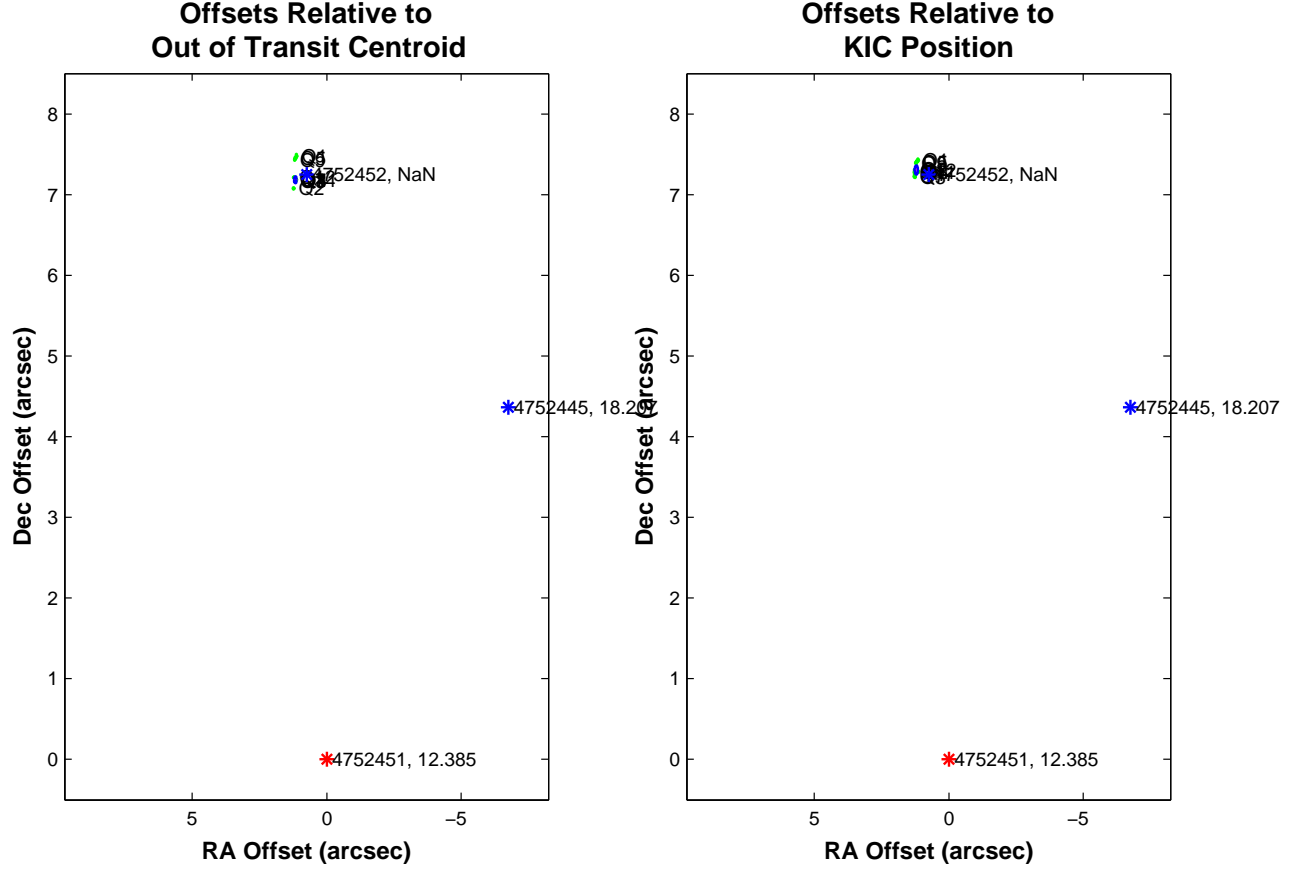


Fig. 19.— An example of multi-quarter offset analysis when the transit signal seems to be on a different star than the target star (KOI-109). The quarterly offsets are tightly clustered around the star KIC 4752452, indicating that this star is the source of the transit. See the caption to Figure 18 for a description of these plots.

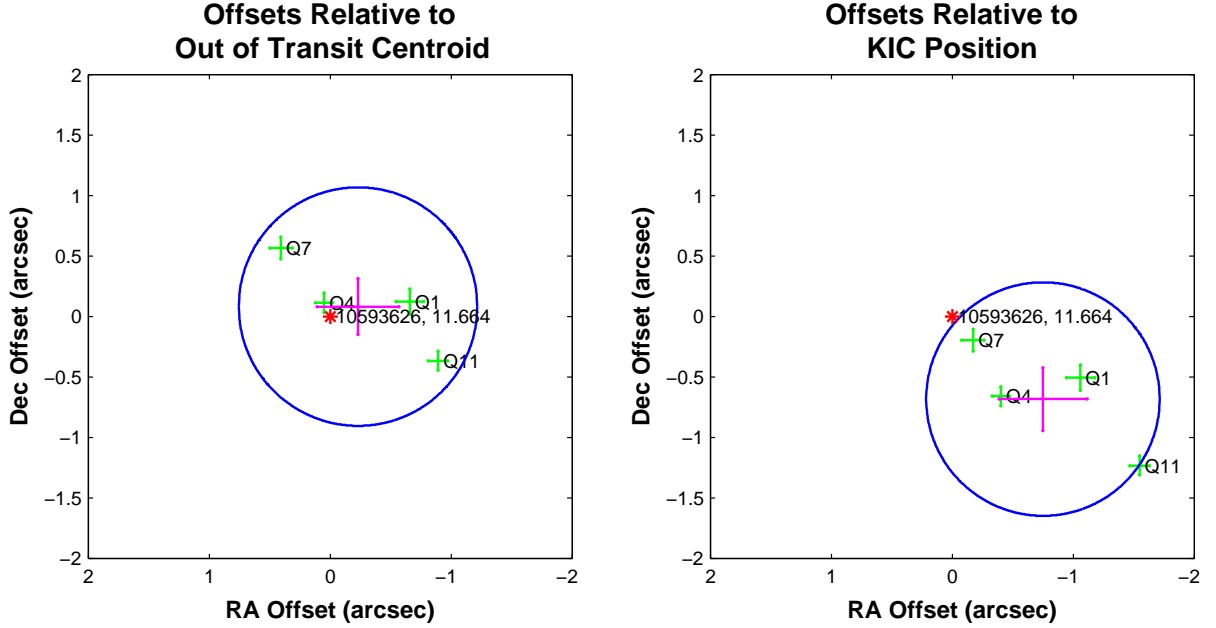


Fig. 20.— An example of multi-quarter offset analysis for a confirmed planet signal (Kepler-22b) with a very long period orbit, so only four quarters show transits. The result is a larger scatter and higher average uncertainty compared to the case where there are transits present in every quarter. Also there is a significant difference in the offsets relative to the out-of-transit centroid in the left panel and relative to the target star’s catalog position in the right panel. This is likely due to a combination of not-fully-averaged PRF bias and catalog error. If this planet were not confirmed by other methods (Borucki, et al. 2012) we would have only moderate confidence that the transit signal is on the target star. See the caption to Figure 18 for a description of these plots.

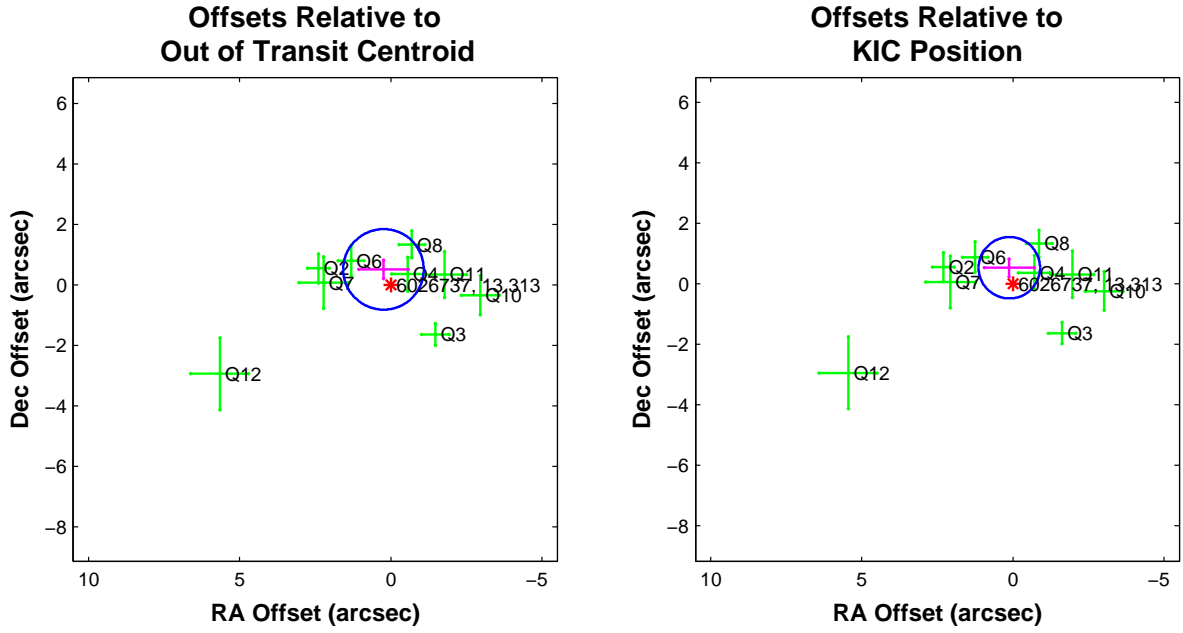


Fig. 21.— An example of multi-quarter offset analysis for a low SNR transit signal (KOI-2949) with $\text{SNR} = 11$. In this case the quarterly offsets have a large scatter measured in arcseconds, but the average across quarters is within 3 standard deviations of the target star. See the caption to Figure 18 for a description of these plots.

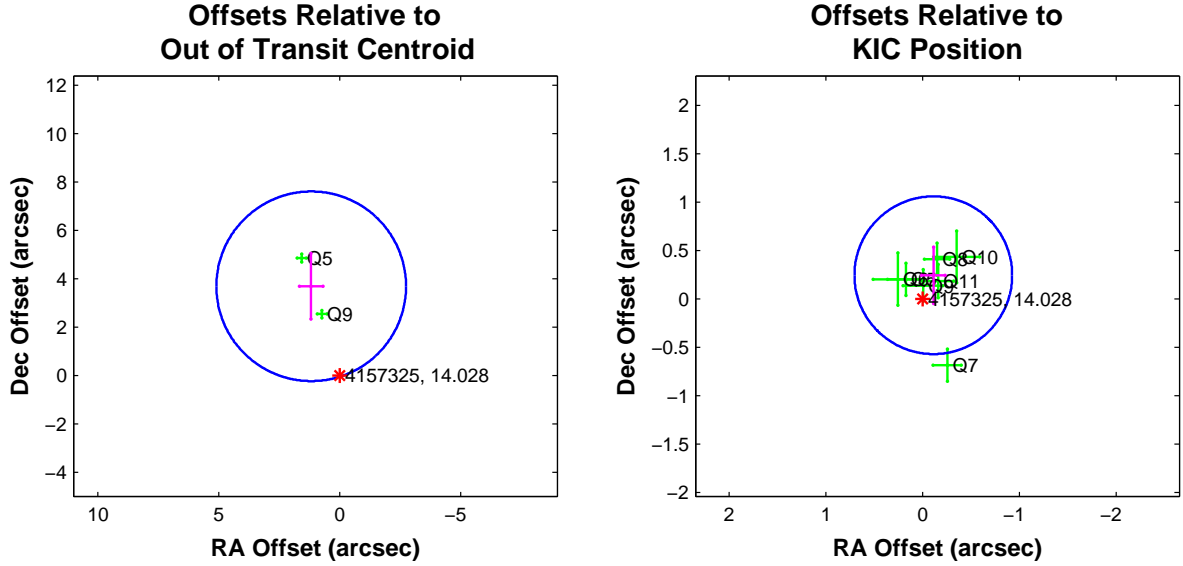


Fig. 22.— An example of multi-quarter offset analysis for a target star (KOI-1860, also discussed in §2.2.1) whose pixels contain a brighter field star (see Figure 17). The offsets relative to the out-of-transit centroid are large because the bright star captured the out-of-transit PRF fit. The out-of-transit PRF fit also failed in many quarters because the bright star is at the edge of the pixel aperture. The offsets relative to the target star’s catalog position are, however, well clustered around the target star indicating that the offset of the transit is not statistically significant. We therefore conclude that the large offset relative to the out-of-transit centroid is due to systematic effects from the bright field star in the pixels. See the caption to Figure 18 for a description of these plots.

have a standard deviation of 0.41 arcseconds. Strong year-to-year correlations prevent the standard deviation from scaling as $1/\sqrt{Q}$, but do not prevent an improvement as Q increases.

Figure 24 shows how the standard deviation depends on the number of quarters averaged. We see that adding a quarter always statistically increases the precision of the multi-quarter average, though this may not be the case for every individual target.

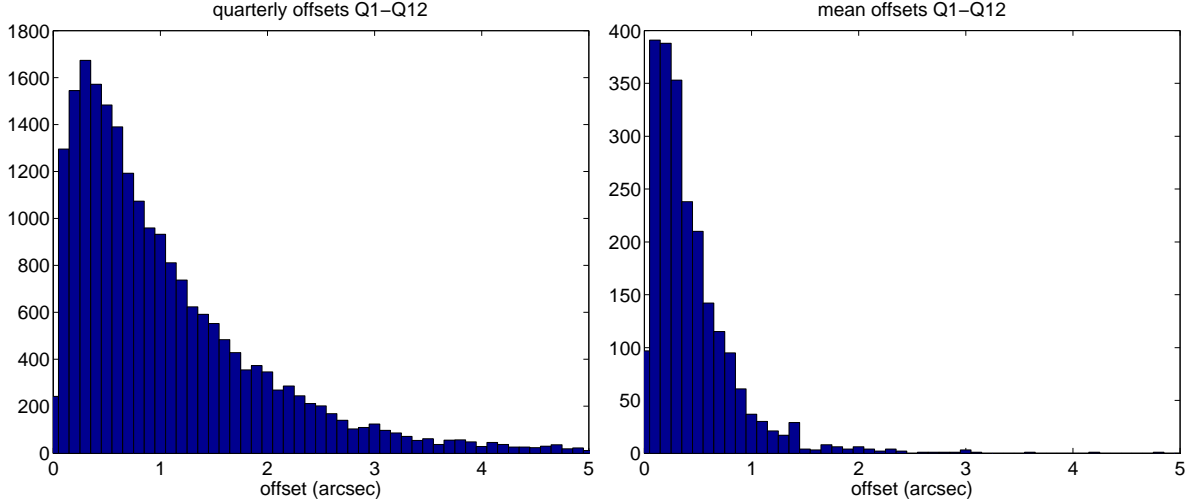


Fig. 23.— Distributions of the PRF-fit offset from the target catalog position for 2,278 KOIs whose quarterly averaged offsets are less than 3σ and whose offsets from the target are < 5 arcseconds. Left: the distribution of individual quarter offsets. Right: the distribution of the multi-quarter averages.

3.4.2. Joint Multi-Quarter PRF Fit

When the transit SNR is very low, there may not be enough signal in each quarterly difference image to support per-quarter PRF fitting. In this case we perform a joint multi-quarter fit, where the pixel images for all quarters are supplied to the PRF fitter, and the single RA and Dec (and quarter-specific PRF amplitude) is found that minimizes the pixel-level difference between the pixel images and PRF-reconstructed pixels over all quarters. In other words, the joint multi-quarter fit finds the single sky position (α, δ) that minimizes the function

$$\chi^2 = \sum_{q=1}^Q \sum_{i=1}^P \frac{1}{\sigma_{p_{i,q}}^2} (p_{i,q} - b_q f_q(\alpha, \delta, r_{i,q}, c_{i,q}))^2 \quad (17)$$

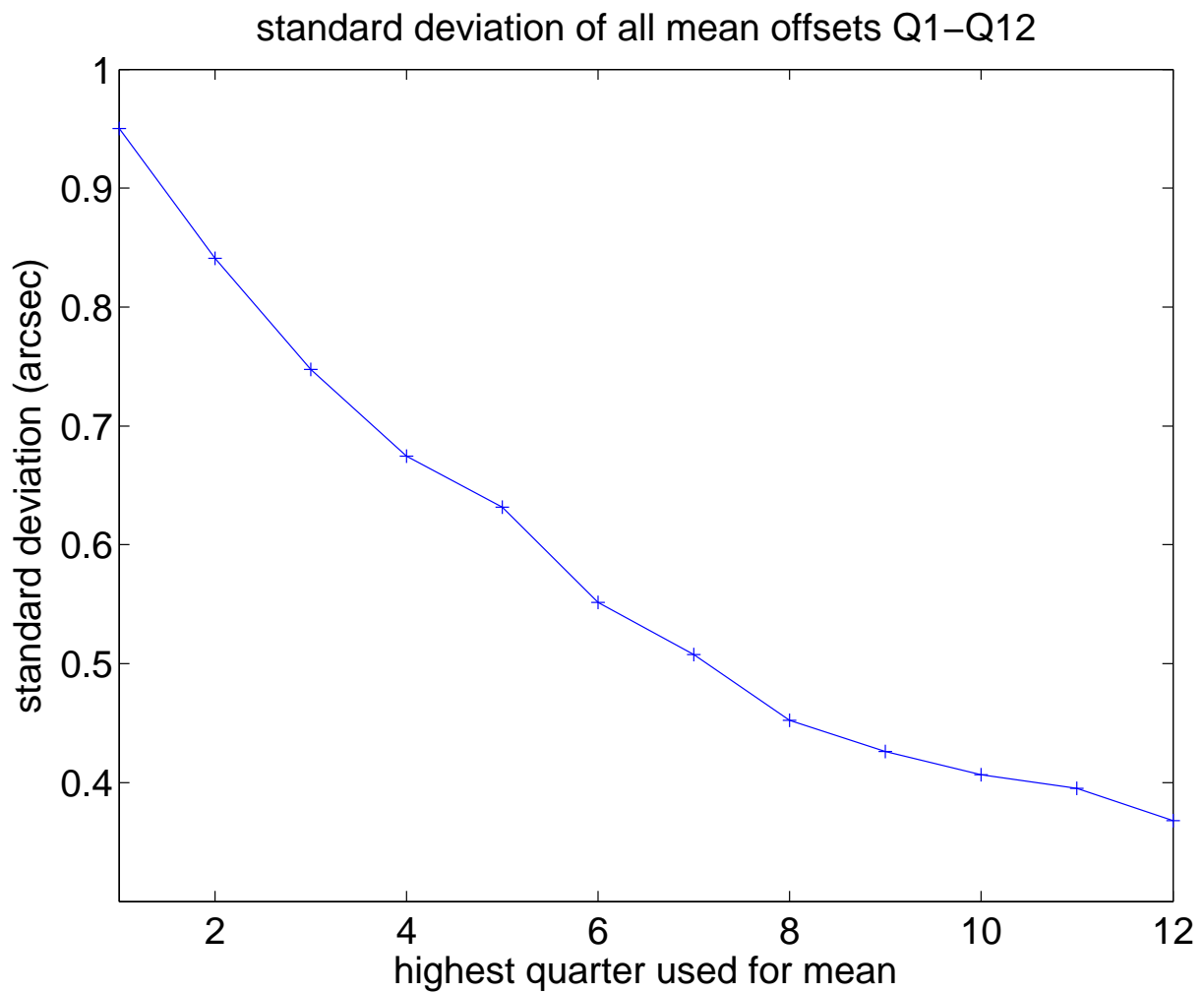


Fig. 24.— The standard deviation of the multi-quarter average as a function of the number of quarters used in the average. The x -axis shows quarters used, where for each point the average is taken for the transits found in quarters 1 through the x -axis value.

where the subscript q means the quarter-specific values of each quantity. So in each quarter the flux-normalized PRF $b_q f_q$ for that quarter is evaluated at (α, δ) (which is common to all quarters) for that quarter’s pixels $(r_{i,q}, c_{i,q})$. These PRF-based pixel values are subtracted from the observed pixel values $p_{i,q}$ for each quarter. The square of this difference normalized by the uncertainty is summed over all the pixels in that quarter, and finally summed over all quarters producing the test χ^2 value. The sky position is varied until the (α, δ) that minimize χ^2 is found. The details of the computation in each quarter are similar to the single-quarter fit in §3.3.

The propagated uncertainty in this fit does not account for scatter across quarters due to systematic error, so it dramatically underestimates the actual uncertainty in this fit. We compute a more accurate uncertainty via a bootstrap approach much like that for the multi-quarter averages described in §3.4.1, except the data consist of pixel images rather than offsets and each element of the ensemble is a joint PRF fit. Specifically, the multi-quarter PRF fit takes as input the set of pixel images (I_1, I_2, \dots, I_Q) constructed in §3.2, where I_q is the pixel image for each quarter. The bootstrap approach creates an ensemble of resamplings-with-replacement sets of pixel images, for example $(I_4, I_5, I_3, I_2, I_2)$ if $Q = 5$. The multi-quarter fit is performed on each element of the ensemble, computing a best fit (α, δ) for each one. Each element of the ensemble is fit with the parameters from the quarter for that component. For example if the first element of the ensemble is I_4 , then the PRF from quarter 4 is applied to those quarter 4 pixels. The uncertainty in the joint multi-quarter fit is then set to the standard deviation of the ensemble of fit positions.

The size of the resampled ensemble needs to be chosen with care. The time to compute the joint multi-quarter fit scales with the number of quarters Q . If the usual choice of Q^2 were chosen for the size of this ensemble, the full computation of the joint fit and its uncertainties would scale as Q^3 . In the *Kepler* pipeline, a bootstrap joint fit of 8 quarters took about 20 minutes, which indicates that a 16-quarter fit would take almost three hours. It is prohibitive to run this on all 15,000 to 20,000 threshold crossing events identified by the pipeline. The joint PRF fit is therefore not routinely run in the *Kepler* pipeline, but is reserved for low SNR transits for which the multi-quarter average does not provide a sufficiently precise result. The possible use of a smaller resampled ensemble is under investigation.

4. Pixel Correlation Images

An alternative method for determining the location of the transit signal in the pixels is to fit the transit model to the individual pixel flux time series. This uses the same fitting method described in §2.2, with the centroid time series replaced by the pixel flux time series.

In this case the fit constant γ is a measure of the presence of the transit signal in each individual pixel. An example of these fits is shown in Figure 25. A *pixel correlation image* can be constructed by setting the value of each pixel to its model fit value γ . When this is done for the example in Figure 25, we get the pixel image in the left panel of Figure 26. The right panel of Figure 26 shows an example where the transit signal is offset from the target star. For such high SNR targets, the transit signal is readily apparent in the pixels, and the correlation image has a star-like appearance. In these cases the photometric or PRF centroiding can be applied to quantitatively and automatically compute the location of the transit, which can be compared to the catalog position of the target star or the target star location from the PRF fit to the difference image.

When the transit has low SNR or the pixels have significant flux from other sources, the pixel correlation image can be of much lower quality. Two examples of this situation are shown in Figure 27.

Because the correlation image is degraded by background flux and can have poor behavior at low SNR, it is not generally used for false positive identification. There are circumstances, however, where the correlation image can be used in combination with the other methods to make a determination. For example, some low SNR targets have marginal difference and correlation images, but if they show the transit signal in the same pixel location then we have increased confidence that the transit signal in those pixels is real.

5. Saturated Targets

Target stars with *Kepler* magnitudes brighter than ~ 11.5 can exhibit saturation, where the flux in a pixel exceeds that pixel’s full well and spills up and down the pixel columns (Caldwell, et al. 2010). The result is that the pixel image of the star can be highly distorted, invalidating all of the centroid methods described in this paper. Saturation can be highly asymmetric, so even photometric centroids are of limited use. Visual inspection of the difference image can, however, reveal large, multi-pixel offsets indicating that the transit is not on the saturating star.

When the saturated star is the transit source, the difference image will have a distinctive, non-star-like, pattern. Because the saturation spills along columns and the amount of spill is approximately proportional to the flux of the star, a transit signal on a saturated star will appear in the difference image as changes at the ends of the saturated columns. An example is shown in Figure 28. This is a characteristic pattern in the difference images for saturated targets. All that can be said in this case is that the transiting source is in approximately the

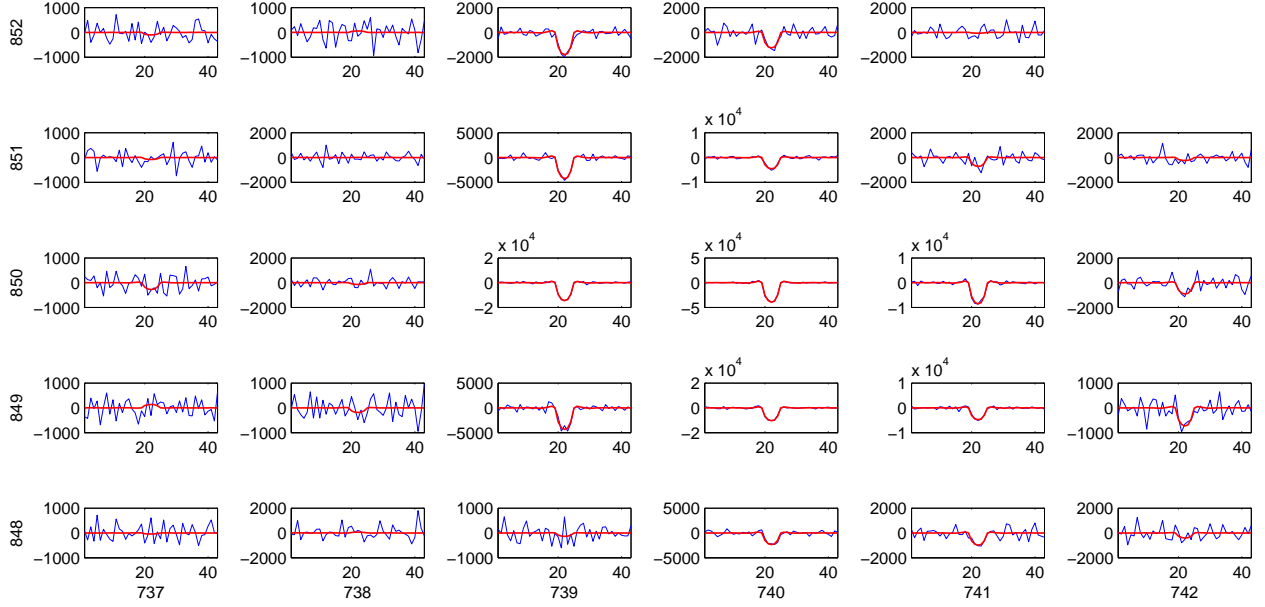


Fig. 25.— Fits of the transit model to individual pixel flux time series for KOI-221 in quarter 7. The pixel flux time series is shown in blue and transit model is in red. Each pixel flux time series is detrended and folded on the transit period. A closeup of the transit event is shown, with the same time interval on all x axes. The y -axes show the pixel values and are scaled to show the variation in each pixel time series. The pixel rows are shown along the left, and pixel columns along the bottom. The pixels that strongly contain the transit signal indicate the location of the transit source.

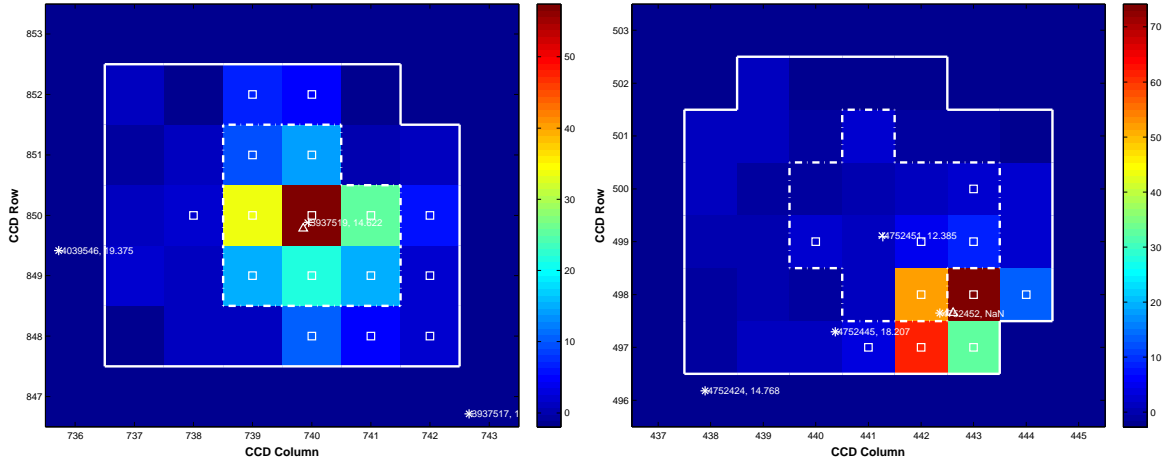


Fig. 26.— Correlation images, created by assigning each pixel the scale factor that multiplies the transit model to best fit that pixel’s flux time series. Left: the example from Figure 25 of the transit signal being coincident with the target star (KOI-221). Right: an example with the transit signal significantly offset from the target star (KOI-109). In these figures the small white squares indicate pixels for which the fit scaling is above a threshold.

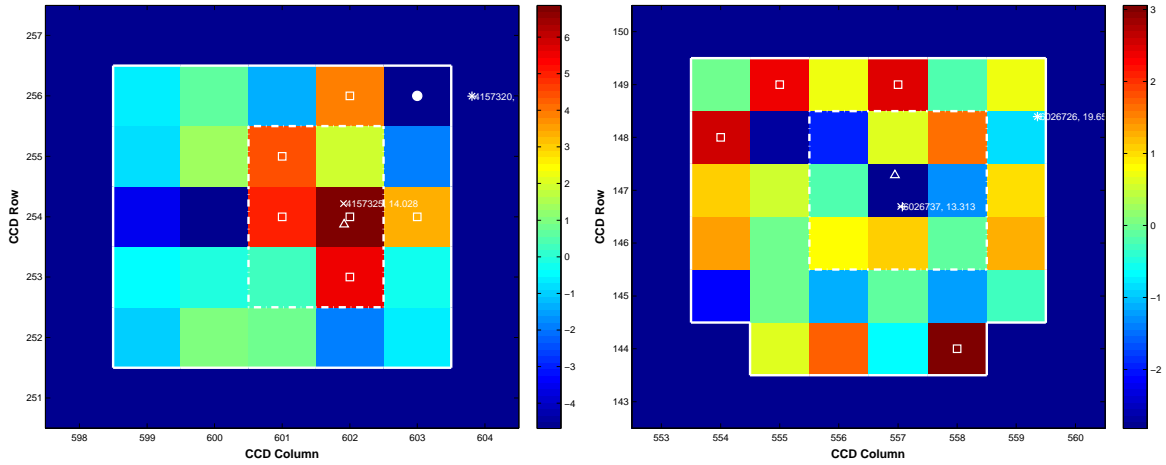


Fig. 27.— Correlation images for more problematic transits. Left: an example where there is a field star in the aperture brighter than the target star (KOI-1860). Variability of the bright star pollutes the correlation image, but the transit signal is still apparent. Right: a low SNR example (KOI-2949) with $\text{SNR} = 11$. For such low SNR transits, the transit signal is barely discernable in the individual pixel time series, which causes the correlation image to be dominated by background variability and pixel-level systematics.

same column position as the target star, between the ends of the saturation. If the transit were due to a field star that is not in the saturated pixels, the difference image would show that star and not the signal from the saturated pixels.

Special investigation of saturated targets can sometimes refine the location of the transit signal. The appearance of the transit at the end of the saturated columns is sensitive to the column position of the transiting source. If the transit SNR is high enough, the wings of the transits can be subject to a PRF fit while masking out the saturated columns. These techniques have been applied with some success, identifying the location of the transit signal to within 4 arcseconds, for Kepler-21b (Howell, et al. 2012). We refer the reader to that publication for details.

6. Performance and Comparison of Techniques

In this section we examine the performance of our transit-source location estimation via photometric and PRF-fit centroids. We focus on offset distances because that is the high-level metric used in initial false positive identification. We examine three populations of targets:

- all Kepler objects of interest (KOIs) dimmer than *Kepler* magnitude 11.5 (to avoid saturated targets (Caldwell, et al. 2010)), which have well-defined transit-like signals of sufficient quality to pass vetting and produce an ephemeris and valid PRF fits (4,049 KOIs). Many of these KOIs are in multiple systems.
- unsaturated KOIs that have been identified as being due to transit sources that are unlikely to be on the target, called Active Pixel Offsets (APOs), that have valid PRF fits as of July 2012 (178 KOIs).
- a small number of APO KOIs whose transit signals have been identified with stars in the *Kepler* input catalog (16 KOIs).

In this section we focus on the following questions:

- How well do the methods identify the location of these sources?
- Is there evidence that the source locations correspond to a uniform distribution of background sources?
- How do these methods compare with one another with respect to accuracy and precision?

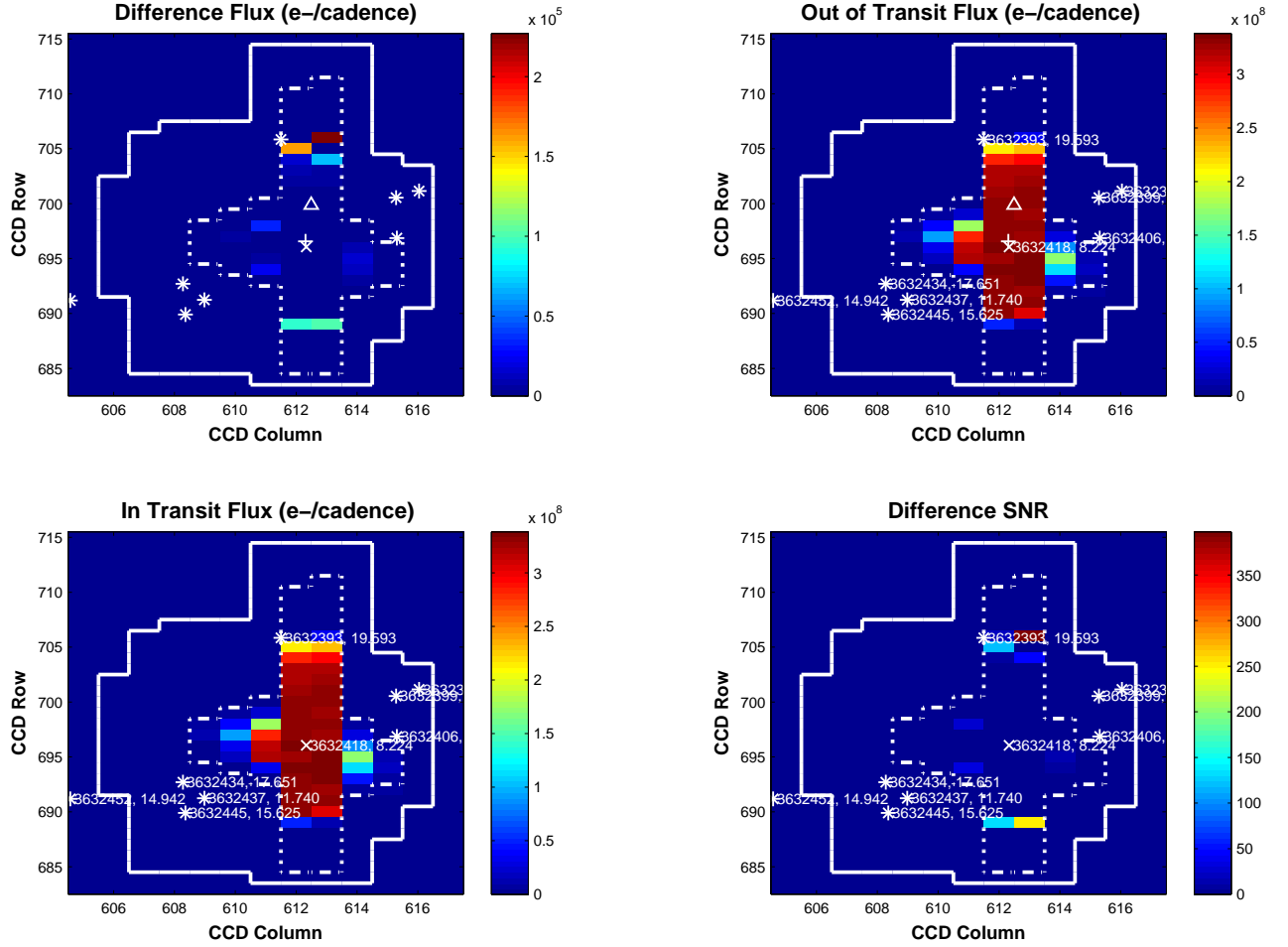


Fig. 28.— An example of a transit signal on a saturated star for the confirmed planet Kepler-21b (Howell, et al. 2012). The host star has *Kepler* magnitude = 8.4 and is highly saturated. In the difference image the transit is apparent in the pixels at the end of the saturation in columns 612 and 613 (the star labels have been removed from the difference image for clarity). The target star is near the boundary between these two columns, which is why there is about equal saturation in both columns. Note the strong asymmetry in the saturation for this quarter, with the saturation going up the columns significantly further than down.

We also address an issue that arises with high-transit-SNR targets, where offsets can be very small but the formal uncertainty can be much smaller. In this situation we encounter residual bias that is not accounted for in the uncertainty, which causes offsets to incorrectly seem statistically significant.

6.1. Accuracy

We use APO targets whose transit signals have been associated with known stars to measure how accurately our two primary methods of photometric and PRF-fit centroids identify the source location. This association is determined by manual investigation of the difference images independently of the offset computations. We see in Figure 29 that the PRF estimate of the transit source offset is close to the star identified as the transit signal source. For APOs with small offsets (< 4 arcseconds) the photometric centroids also have good accuracy. For APOs with larger offsets, however, photometric centroids show large errors. This behavior is expected because the *Kepler* pipeline uses one set of pixels to estimate the depth of the transit signal and a larger set of pixels to compute the photometric centroid. As described in §2.3.1, when the transit source has significant flux that falls outside the pixels used for the depth estimate, which is the case when the source is more than 4 arcseconds from the target star, there can be significant error in the transit source location inferred from the photometric centroids.

Figure 30 compares the PRF-fit and photometric centroid source offset estimates for all KOIs, and shows that the photometric centroid estimate of the source offset is generally (but not always) larger than the PRF-fit estimate when the PRF-fit source location source is more than a few arcsec from the target.

Figure 31 compares the PRF-fit source offset relative to the target star catalog position with the PRF-fit source offset relative to the out-of-transit PRF-fit centroid. These two offsets are similar for the majority of stars, with outliers that are likely due to bias due to crowding.

Figure 32 compares the distribution of the APO KOIs and the distribution of observed pixel area relative to target stars. The fact that these two distributions have similar shapes with similar peaks is consistent with the identified APOs representing a uniform background of eclipsing binaries and possibly large planetary transits. This consistency contributes to our confidence that the APOs are correctly identifying astrophysical false positives.

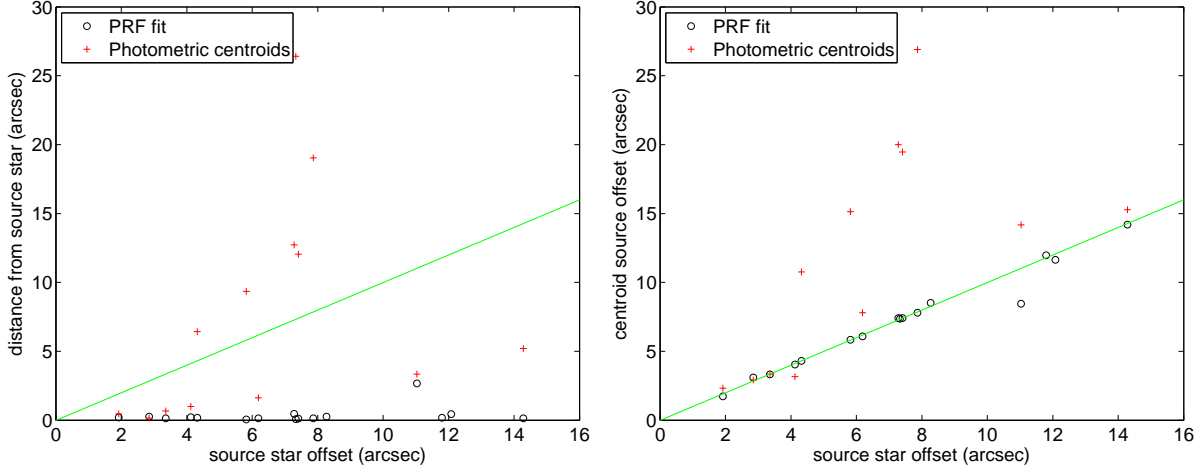


Fig. 29.— Left: The distance of the PRF-fit and photometric centroids from known stars that are likely to be the source of confirmed APO transit signals (y -axis) vs. the distance of the known star from the target star (x -axis). Right: the same stars, showing the offset of the centroid from the target star (y -axis). The PRF offsets are relative to the target star catalog location for consistency with the photometric offsets.

6.2. Precision vs. SNR

The precision of a centroid measurement is dependent on the strength of the transit signal in each pixel. This strength depends on the transit depth, host star brightness and number of transits among other factors. All of these factors contribute to the transit SNR, so we analyze precision as a function of transit SNR. Figure 33 shows the dependence of formal centroid source offset uncertainty on transit SNR. Both the PRF-fit and photometric centroid methods show similar dependencies, though the uncertainties for the PRF-fit centroid method is somewhat smaller. A linear fit to the log-log data gives the uncertainty of the two methods as

$$\sigma_{\text{photometric}} = \frac{13.6 \pm 0.16}{(\text{SNR})^{1.05 \pm 0.00}}, \quad \sigma_{\text{PRF-fit}} = \frac{3.39 \pm 0.10}{(\text{SNR})^{0.89 \pm 0.01}}. \quad (18)$$

These fits, along with the range of values implied by the $1\text{-}\sigma$ uncertainties in the fit parameters, are shown in Figure 34. The uncertainty of the photometric centroid method is inversely proportional to the SNR, as expected, while the PRF-fit method has a somewhat smaller dependence on inverse SNR. The coefficient of these uncertainties (13.6 for photometric uncertainties and 3.39 for the PRF fit) is larger than the full-width-half-max expected for centroid uncertainties because these uncertainties include contributions from the offset computation. The uncertainties reported in this section are propagated formal uncertain-

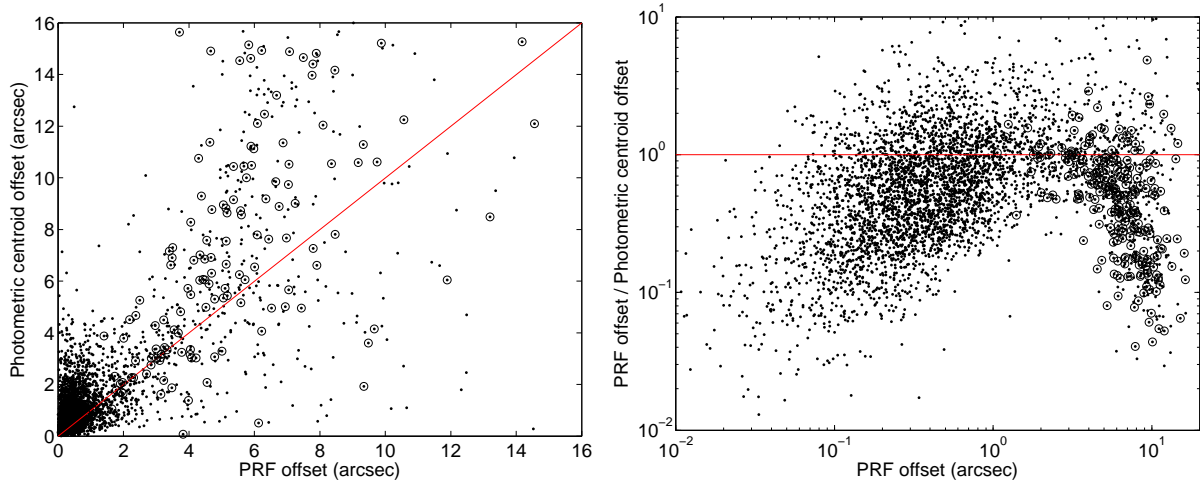


Fig. 30.— Left: A comparison between the PRF-fit offsets (x -axis) and the photometric centroid source offsets (y -axis) from the target star catalog position. Right: The ratio PRF-fit offsets/photometric centroid source offsets (y -axis) vs. magnitude of the PRF-fit offsets (x -axis). APO KOIs are marked by circles. The red line in both figures indicates equality between the PRF-fit and photometric offsets. We see that the photometric centroid estimate of the source distance agrees with the PRF estimate for distances of a few arcsec from the target star. As expected, the photometric centroid usually overestimates the offset for transit sources that are further from the target star (see §2.3.1).

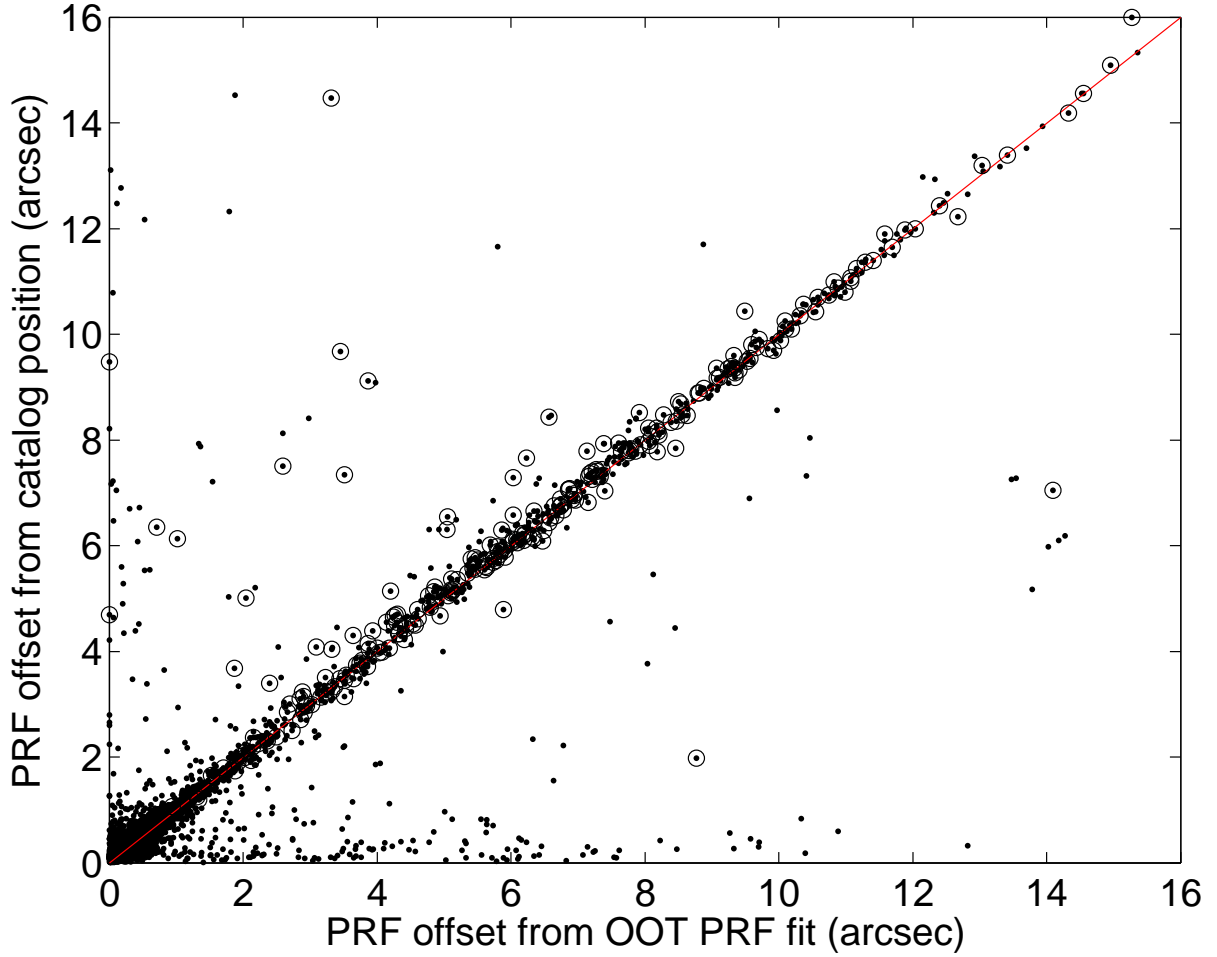


Fig. 31.— A comparison of the PRF-fit source offset relative to the PRF fit to the out-of-transit pixel image (x -axis) and the PRF-fit source offset relative to the catalog position of the target star. APO KOIs are marked by circles. We see that most targets with large offsets cluster along the diagonal indicating that the two offsets are generally in reasonable agreement. Outliers are likely due to crowding issues.

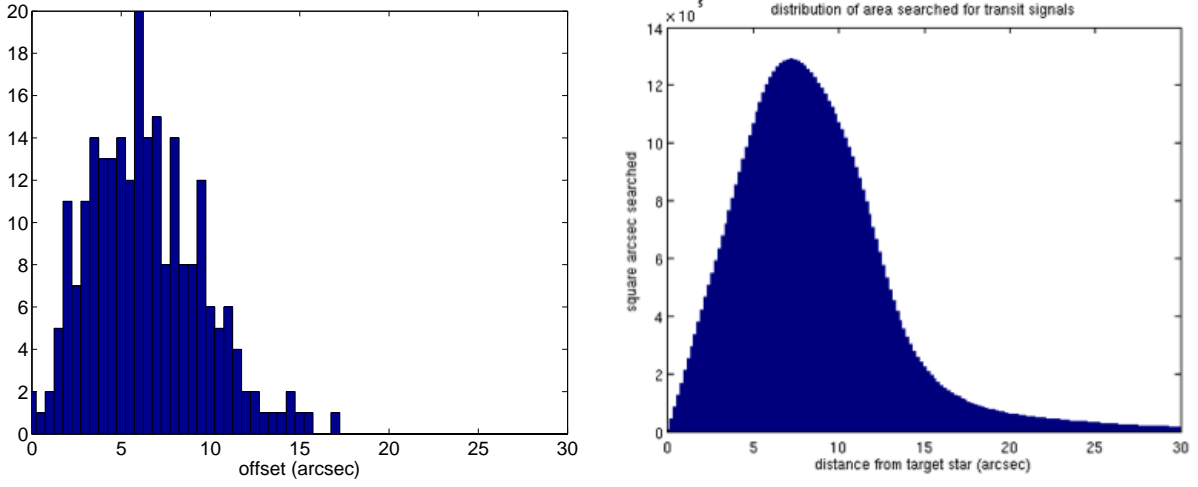


Fig. 32.— Left: the distribution of PRF-fit source offsets for targets identified as APOs. There is a strong peak at about 6-7 arcseconds. This distribution is strongly dependent on the pixel aperture associated with each target star, which limits the offset that can be detected. Right: the distribution of pixel area as a function of distance from the target star associated with each pixel, across the *Kepler* field of view. This distribution also a peak at about 7 arcseconds. The similarity between these two distributions is consistent with the identified APOs representing a uniform distribution of background sources such as eclipsing binaries and large transiting planets.

ties, however, which are only valid if all noise sources are zero-mean Gaussian white noise. As described in this paper there are several sources of systematic error that impact transit source offset estimation. These systematic errors are not reflected in the formal uncertainty.

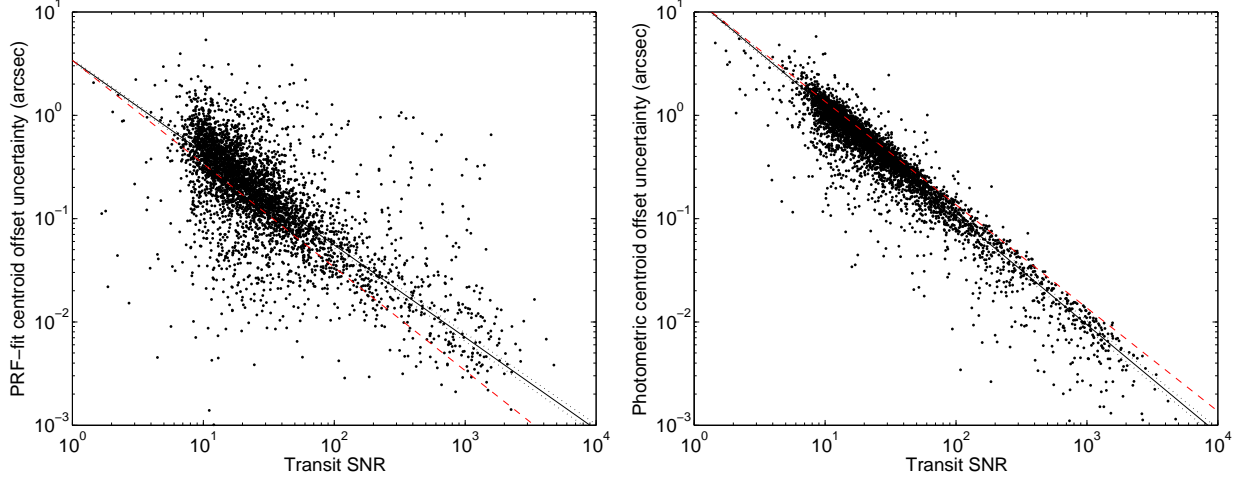


Fig. 33.— Formal offset uncertainty vs. transit SNR for PRF fit (left) and photometric (right) centroids using 12 quarters of data. The red dashed line in both figures shows the $1/\text{SNR}$ dependency for comparison. We see that the precision of the PRF-fit offsets is somewhat better on average than the PRF fit offsets. This precision does not account for bias due to systematic error for either type of centroid.

Because the dependence of the PRF-fit and photometric centroid estimates of the source offset on SNR have similar log slopes we expect that if one technique indicates a significant offset then the other technique will as well. This is shown in Figure 35, which indicates that for most targets the photometric centroid and PRF-fit methods are in agreement as to whether there is a significant offset for a particular target. But there are many targets, including a few identified APOs, that have photometric centroid source offsets $< 3\sigma$ but PRF-fit source offsets $> 3\sigma$ and vice versa.

Quantitatively, for 54.9% of all KOIs the two techniques are in agreement that the source offset is $< 3\sigma$; 24.7% of all KOIs have agreement that the source offset is $> 3\sigma$; 13.9% of all KOIs have offsets $> 3\sigma$ according to the PRF-fit technique but $< 3\sigma$ according to photometric centroids; and 6.45% of all KOIs have offsets $< 3\sigma$ according to the PRF-fit technique but $> 3\sigma$ according to photometric centroids. Therefore the two methods are in agreement on significance for about 80% of the targets. Most of the targets for which the PRF-fit techniques indicate an offset $> 3\sigma$ but the photometric centroids have a shift $< 3\sigma$ have very small PRF-fit offsets, so they are at distances where residual bias dominates as

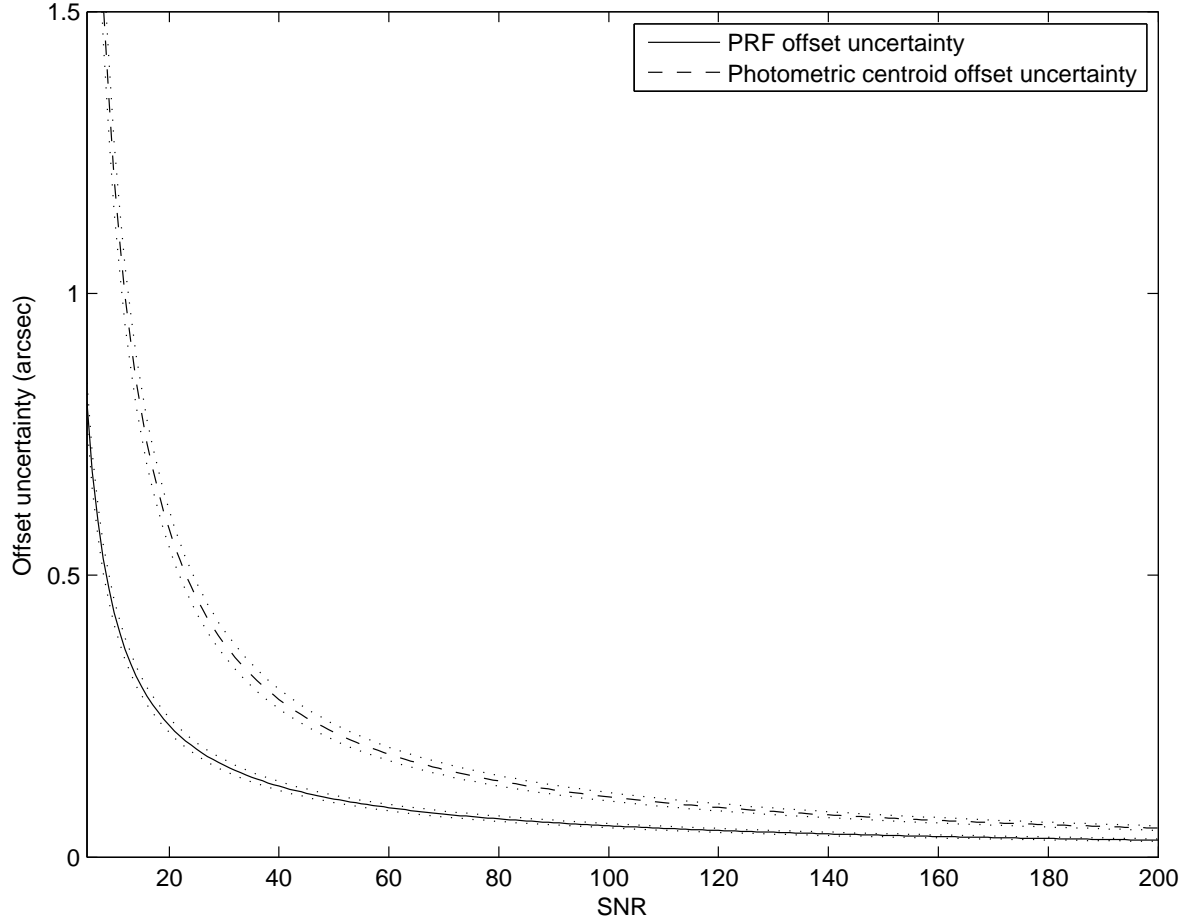


Fig. 34.— Uncertainty vs. SNR from the fits in Figure 33 plotted on linear scales. The dotted lines indicate the range of variation due to the 1- σ uncertainties in the fit parameters.

discussed in §6.3.

6.3. Residual Bias and High SNR Transits

As described in §3.3.1, the computation of the PRF-fit source offset is subject to various kinds of bias due to PRF error and crowding. When the transit SNR is high, both centroid methods will have very high formal precision with very small uncertainties. The PRF-fit source offset estimate essentially hits a noise floor, where the offsets are dominated by residual biases. Figure 36 shows that this noise floor begins to be apparent at source offsets of about 2 arcseconds, where there is a noticeable increase in objects with offsets between 3 and 4σ . Below about 0.2 arcseconds there is a large excess of objects with large offsets in units of σ . The right panel of Figure 36 shows targets with high SNR. In this population offsets are mostly very small, and we find most of the large excess of high- σ offsets. We interpret this to mean that residual biases in the PRF-fit source offset are dominant under 0.2 arcseconds.

Figure 37 shows a similar analysis for photometric-centroid-based source offsets. The excess of significantly offset targets is apparent but less severe in this case.

We mitigate the impact of residual bias on small offset / high SNR targets in PRF-fit estimates of the source offset in two ways:

- Adding a small constant "noise floor" to reflect the residual bias. Because bias seems to dominate at less than 0.2 arcseconds, we want to avoid classifying any target with a source offset less than 0.2 arcseconds as an APO false positive. Because this classification is based on a 3σ threshold we add $\sigma_0 = 0.2/3$ arcseconds in quadrature to the formal uncertainty in each component: $\sigma_{\Delta\alpha} \rightarrow \sqrt{\sigma_{\Delta\alpha}^2 + \sigma_0^2}$, $\sigma_{\Delta\delta} \rightarrow \sqrt{\sigma_{\Delta\delta}^2 + \sigma_0^2}$. (This has the same effect on the offset distance uncertainty σ_D as adding σ_0 to σ_D in quadrature). The impact of adding this noise floor is shown in Figure 38.
- Special treatment is given to vetting targets with small source offsets. An example simple set of rules for manual vetting for false positives is the following:
 - pass all targets with offsets < 0.2 arcseconds (this happens automatically when using the above noise floor)
 - for targets with offsets < 1 arcsecond, manually investigate those targets with offsets > 3σ
 - for targets with offsets between 1 and 2 arcseconds, manually investigate those targets with offsets between 3 and 4σ

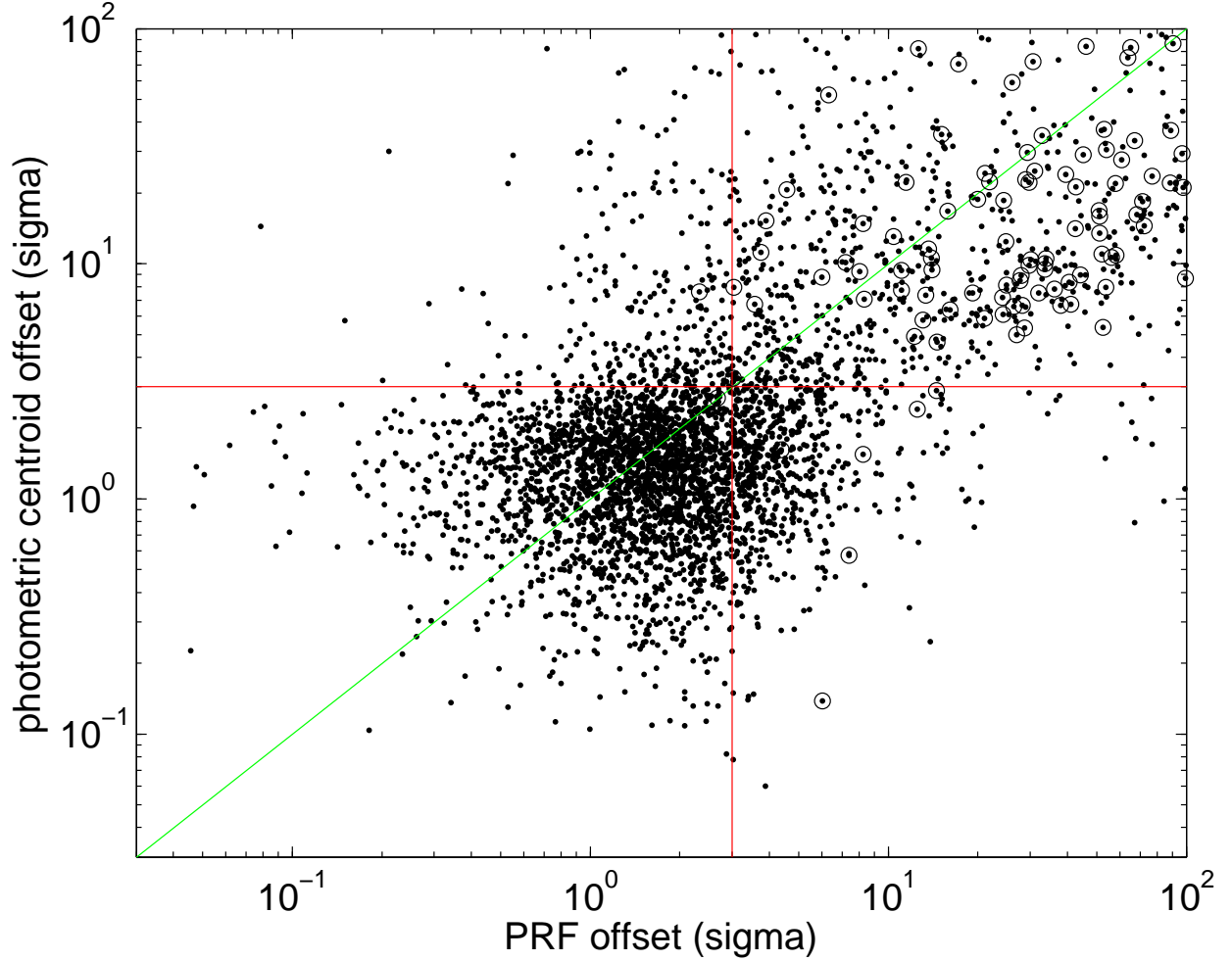


Fig. 35.— A comparison of the PRF-fit source offset relative to the catalog position of the target star (x -axis) and the photometric centroid source offset (y -axis), both in units of σ . The vertical and horizontal lines mark where the offset $= 3\sigma$, above which the offset is considered statistically significant. APO KOIs are marked by circles. We see that most targets have both offsets below 3σ , but there are a significant number of targets for which the photometric centroid source offset is less than 3σ but the PRF-fit offset is $> 3\sigma$ and vice versa.

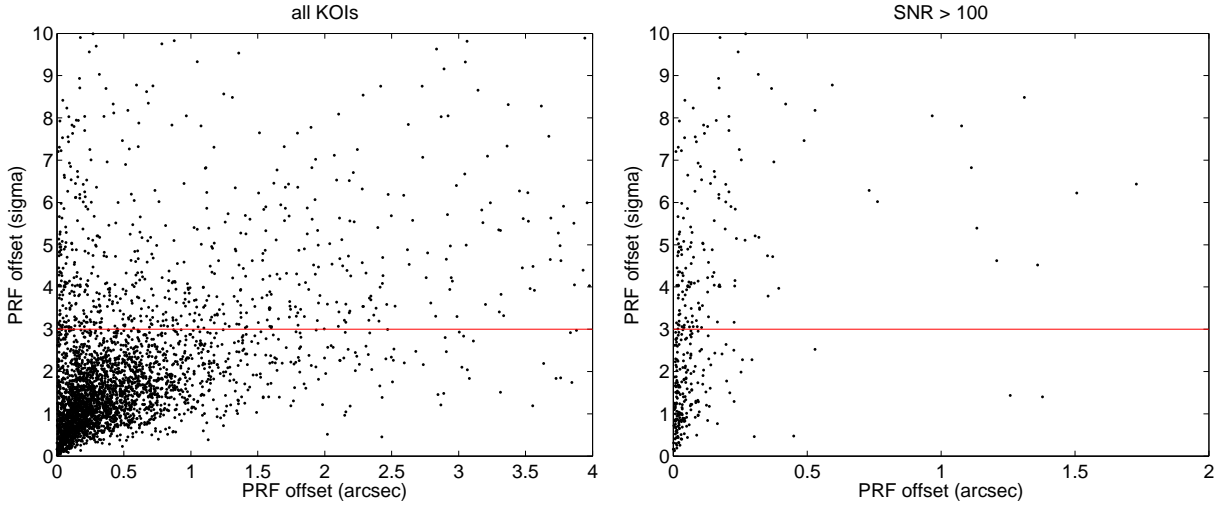


Fig. 36.— The relationship between the PRF-fit source offset (x -axis) and source offset in units of sigma (y -axis). Left: all KOIs. Right: KOIs with transit SNR > 100 . On the left we see that for offsets < 3 arcseconds there seem to be an excess of targets with offset $> 3\sigma$ (red line). On the right we see that for high SNR targets the offset is small, but there is an excess of targets with offset $> 3\sigma$. This is likely due to residual bias from the errors discussed in §3.3.1.

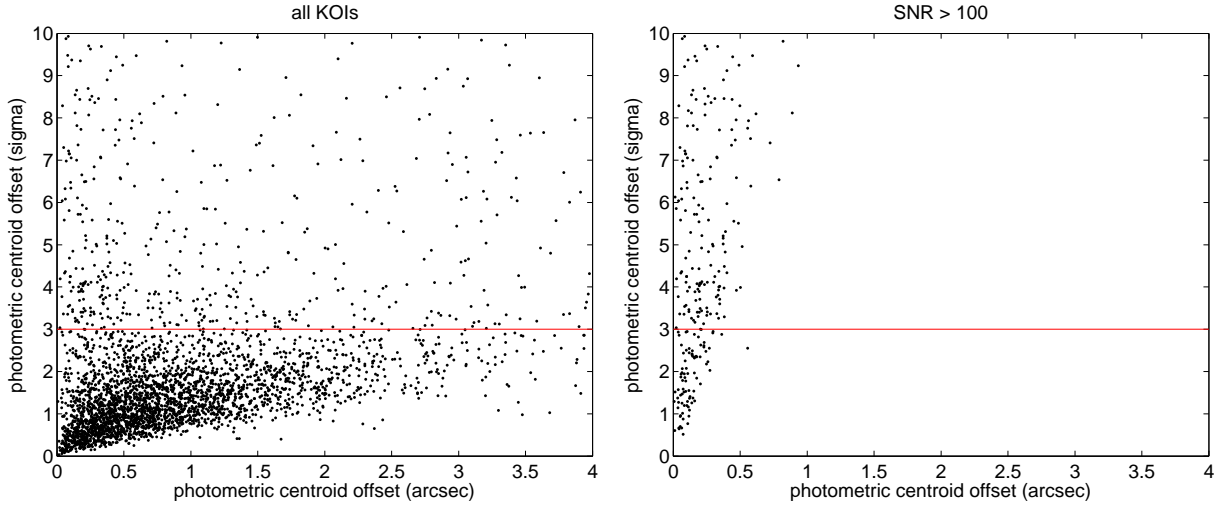


Fig. 37.— The relationship between the photometric centroid source offset (x -axis) and source offset in units of sigma (y -axis). Left: all KOIs. Right: KOIs with transit SNR > 100 . Many KOIs fall outside the plot, but our interest is in small offset behavior. On the left we see that for offset < 0.2 arcseconds there seem to be an excess of targets with offset $> 3\sigma$ (red line). On the right we see that for high SNR targets the offset is small, but there is an excess of targets with offset $> 3\sigma$.

- for targets with offsets between 1 and 2 arcseconds, declare as APO targets with offsets above 4σ
- for targets with offsets > 2 arcseconds, declare as APO targets with offsets above 3σ

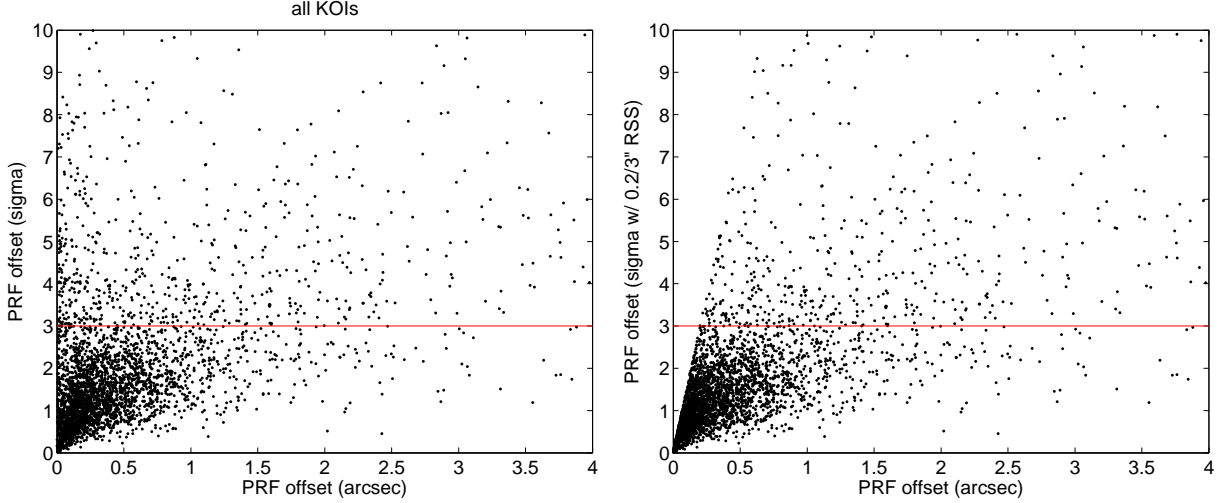


Fig. 38.— The effect of adding a small constant to the PRF-fit source offset uncertainty on the relationship between the PRF-fit source offset (x -axis) and source offset in units of sigma (y -axis). Left: all KOIs from Figure 36. Right: the same targets with a constant 0.2/3 arcseconds added to the formal uncertainty in quadrature. The excess of targets exceeding 3σ at offset < 0.2 sigma has been removed.

7. Conclusions

Many background astrophysical false positives can be identified through centroid analysis of *Kepler* pixel data. The high photometric precision of the *Kepler* data provides opportunities to identify such objects close to the target star, but great care must be taken to account for various systematic biases. We have presented three different techniques, two of which were analyzed in detail. This ensemble provides a power arsenal of tools for dispositioning nearly all KOIs.

The PRF fit technique provides the best accuracy in the localization of transit sources that are not on the target star. The photometric centroid technique behaves best when the target star is isolated and the transit source is close to (or is) the target star. The

photometric centroid technique is therefore useful for confirming that the transit is on the target star when this is also indicated by the PRF fit technique. The photometric centroid technique can indicate when the transit source is separated from the target star, but when the separation is more than a few arcseconds the source location determined by photometric centroids is unreliable.

When the SNR is low or there is significant crowding, the PRF technique can break down. In this case the photometric technique may provide the best evidence that the centroid is on the target star. The pixel correlation images can also be useful in this circumstance, though the pixel correlation technique is fragile.

We find that we often use all three techniques when investigating a difficult target. This toolbox of techniques is a critical component of the *Kepler* planet candidate vetting process and makes a significant contribution to the reliability of the *Kepler* planet candidate list.

8. Acknowledgements

We gratefully acknowledge the outstanding work of the entire *Kepler* team that performs the data acquisition and analysis, and delivers the precision that makes the techniques described in this paper possible. We particularly thank the *Kepler* Science Operations Center and Science Office for their support and creativity while these techniques were being developed. We thank Martin Still, Susan Thompson and Jeff Coughlin for valuable comments on early drafts of this paper. Finally we thank Bill Borucki, Ted Dunham, Dave Latham, Nick Gautier and the wider *Kepler* science community for constant support and encouragement.

Kepler was competitively selected as the tenth Discovery mission. Funding for this mission is provided by NASA’s Science Mission Directorate.

Facilities: The Kepler Mission

A. Derivation of the formula relating centroid shifts to transit source location

Assume that we are observing a target star with flux b_0 at (α_0, δ_0) , with N nearby stars at RA and Dec (α_j, δ_j) , $j = 1, \dots, N$, and flux b_j . Assume the star k , with $k \neq 0$, is a background eclipsing binary with fractional eclipse depth d_{back} (so the flux of star k in mid eclipse is $(1 - d_{\text{back}})b_k$). We model the PSF of the star with a function $f(\alpha, \delta)$ that has the following properties, where the integral is taken over the domain where $f > 0$:

- $f(\alpha, \delta)$ has finite support ($f = 0$ outside of a finite area).
- $\int f(\alpha, \delta) d\alpha d\delta = 1$. In other words f has unit flux so $b_j f$ has the total flux

$$\int b_j f(\alpha, \delta) d\alpha d\delta = b_j.$$

- $\int \alpha f(\alpha - \alpha_j, \delta - \delta_j) d\alpha d\delta = \alpha_j$ and $\int \delta f(\alpha - \alpha_j, \delta - \delta_j) d\alpha d\delta = \delta_j$ so, for example,

$$\frac{\int \alpha b_j f(\alpha - \alpha_j, \delta - \delta_j) d\alpha d\delta}{\int b_j f(\alpha - \alpha_j, \delta - \delta_j) d\alpha d\delta} = \frac{\alpha_j b_j}{b_j} = \alpha_j,$$

so the centroid of an isolated star is the same as that star's position.

We now consider an aperture on the sky that may not completely capture all flux from stars in the aperture, and may contain flux from stars outside the aperture. Therefore $\int_{\text{ap}} b_j f(\alpha, \delta) d\alpha d\delta \neq b_j$, $\int_{\text{ap}} \alpha f(\alpha - \alpha_k, \delta - \delta_k) d\alpha d\delta \neq \alpha_k$ and $\int_{\text{ap}} \delta f(\alpha - \alpha_k, \delta - \delta_k) d\alpha d\delta \neq \delta_k$, where \int_{ap} denotes an integral over the aperture. We model the background flux as an arbitrary function $B(\alpha, \delta)$. We denote the total flux in the aperture by

$$F^{\text{ap}} = \int_{\text{ap}} \left(\sum_{j=1}^N b_j f(\alpha - \alpha_j, \delta - \delta_j) + B(\alpha, \delta) \right) d\alpha d\delta.$$

To simplify the following discussion, we define the notation

$$\begin{aligned} I_j^{\text{ap}} &:= \int_{\text{ap}} f(\alpha - \alpha_j, \delta - \delta_j) d\alpha d\delta, & B^{\text{ap}} &:= \int_{\text{ap}} B(\alpha, \delta) d\alpha d\delta, \\ I_j^{\text{ap}, \alpha} &:= \int_{\text{ap}} \alpha f(\alpha - \alpha_j, \delta - \delta_j) d\alpha d\delta, & I_j^{\text{ap}, \delta} &:= \int_{\text{ap}} \delta f(\alpha - \alpha_j, \delta - \delta_j) d\alpha d\delta, \\ B^{\text{ap}, \alpha} &:= \int_{\text{ap}} \alpha B(\alpha, \delta) d\alpha d\delta, & B^{\text{ap}, \delta} &:= \int_{\text{ap}} \delta B(\alpha, \delta) d\alpha d\delta \end{aligned}$$

So $b_j I_j^{\text{ap}}$ is the flux from star j in the aperture, B^{ap} is the background flux in the aperture, and the superscript α or δ indicates the first moment in RA or Dec of these quantities. Then $F^{\text{ap}} = \sum_{j=1}^N b_j I_j^{\text{ap}} + B^{\text{ap}}$.

The out-of-transit centroid (including all flux in the aperture) is given by

$$C_{\alpha}^{\text{out}} = \frac{\sum_{j=1}^N b_j I_j^{\text{ap}, \alpha} + B^{\text{ap}, \alpha}}{F^{\text{ap}}}, \quad C_{\delta}^{\text{out}} = \frac{\sum_{j=1}^N b_j I_j^{\text{ap}, \delta} + B^{\text{ap}, \delta}}{F^{\text{ap}}}.$$

The in-transit centroid is given by

$$\begin{aligned}
C_\alpha^{\text{in}} &= \frac{\sum_{j=1, j \neq k}^N b_j I_j^{\text{ap}, \alpha} + B^{\text{ap}, \alpha} + (1 - d_{\text{back}}) b_k I_k^{\text{ap}, \alpha}}{\sum_{j=1, j \neq k}^N b_j I_j^{\text{ap}} + B^{\text{ap}} + (1 - d_{\text{back}}) b_k I_k^{\text{ap}}} \\
&= \frac{C_\alpha^{\text{out}} F^{\text{ap}} - d_{\text{back}} b_k I_k^{\text{ap}, \alpha}}{F^{\text{ap}} - d_{\text{back}} b_k I_k^{\text{ap}}}, \\
C_\delta^{\text{in}} &= \frac{C_\delta^{\text{out}} F^{\text{ap}} - d_{\text{back}} b_k \delta_k}{F^{\text{ap}} - d_{\text{back}} b_k I_k^{\text{ap}}}.
\end{aligned}$$

The observed depth is defined so that the observed flux in mid eclipse is $(1 - d_{\text{obs}}) F^{\text{ap}}$. Assuming that the eclipse is the only cause of a change in flux, the observed flux in mid eclipse is also given by $F^{\text{ap}} - d_{\text{back}} b_k I_k^{\text{ap}}$. Therefore $(1 - d_{\text{obs}}) F^{\text{ap}} = F^{\text{ap}} - d_{\text{back}} b_k I_k^{\text{ap}}$, so $d_{\text{obs}} = \frac{d_{\text{back}} b_k I_k^{\text{ap}}}{F^{\text{ap}}}$.

The centroid shift is given by

$$\begin{aligned}
\frac{\Delta C_\alpha}{\cos \delta} &= C_\alpha^{\text{in}} - C_\alpha^{\text{out}} \\
&= \frac{C_\alpha^{\text{out}} F - d_{\text{back}} b_k I_k^{\text{ap}, \alpha} - C_\alpha^{\text{out}} F^{\text{ap}} + C_\alpha^{\text{out}} d_{\text{back}} b_k I_k^{\text{ap}}}{F^{\text{ap}} - d_{\text{back}} b_k I_k^{\text{ap}}} \\
&= -\frac{d_{\text{back}} b_k I_k^{\text{ap}, \alpha} - C_\alpha^{\text{out}} I_k^{\text{ap}}}{F^{\text{ap}} (1 - d_{\text{obs}})} \\
&= -\frac{d_{\text{obs}}}{1 - d_{\text{obs}}} \frac{I_k^{\text{ap}, \alpha} - C_\alpha^{\text{out}} I_k^{\text{ap}}}{I_k^{\text{ap}}} \\
&= -\frac{d_{\text{obs}}}{1 - d_{\text{obs}}} \left(\frac{I_k^{\text{ap}, \alpha}}{I_k^{\text{ap}}} - C_\alpha^{\text{out}} \right), \\
\Delta C_\delta &= -\frac{d_{\text{obs}}}{1 - d_{\text{obs}}} \left(\frac{I_k^{\text{ap}, \delta}}{I_k^{\text{ap}}} - C_\delta^{\text{out}} \right).
\end{aligned}$$

We define

$$C_k^{\text{ap}, \alpha} = \frac{I_k^{\text{ap}, \alpha}}{I_k^{\text{ap}}}, \quad C_k^{\text{ap}, \delta} = \frac{I_k^{\text{ap}, \delta}}{I_k^{\text{ap}}},$$

which are the RA and Dec of the centroid of the flux of the transit source k in the aperture when all other flux is absent (alternatively this is the centroid of the difference image formed by subtracting in-transit pixels from out-of-transit pixels when all other flux is constant). Therefore this centroid is given by

$$C_k^{\text{ap}, \alpha} := C_\alpha^{\text{out}} - \left(\frac{1}{d_{\text{obs}}} - 1 \right) \frac{\Delta C_\alpha}{\cos \delta}, \quad C_k^{\text{ap}, \delta} := C_\delta^{\text{out}} - \left(\frac{1}{d_{\text{obs}}} - 1 \right) \Delta C_\delta. \quad (\text{A1})$$

$(C_k^{\text{ap},\alpha}, C_k^{\text{ap},\delta})$ approximate the transit source location (α_k, δ_k) , with the error in this approximation decreasing as more flux from the transit source is captured in the aperture. When all flux from the transit source is captured in the aperture, $(C_k^{\text{ap},\alpha}, C_k^{\text{ap},\delta}) = (\alpha_k, \delta_k)$.

In the *Kepler* pipeline implementation, the transit depth is estimated using the optimal aperture (Bryson, et al. 2010) while the centroids are measured using the optimal aperture plus a one-pixel ring around the optimal aperture. This is because some optimal apertures consist of only a single pixel, which cannot be usefully centroided. This use of one aperture for centroid computation and a smaller aperture to estimate observed transit depth invalidates the conclusion of the above analysis because d_{obs} in Equation (A1) is different from the depth $d_{\text{obs}}^{\text{optAp}}$ determined using the optimal aperture.

We can estimate the difference in these observed depths and predict the impact on the estimated transit source position. For the aperture used for centroiding, we have the relation $d_{\text{obs}} F^{\text{ap}} = d_{\text{back}} b_k I_k^{\text{ap}}$, while for the optimal aperture we have the same relation: $d_{\text{obs}}^{\text{optAp}} F^{\text{optAp}} = d_{\text{back}} b_k I_k^{\text{optAp}}$. Solving both relations for $d_{\text{back}} b_k$ and equating, we find

$$\frac{d_{\text{obs}} F^{\text{ap}}}{I_k^{\text{ap}}} = \frac{d_{\text{obs}}^{\text{optAp}} F^{\text{optAp}}}{I_k^{\text{optAp}}} \Rightarrow d_{\text{obs}}^{\text{optAp}} = d_{\text{obs}} \frac{F^{\text{ap}}}{F^{\text{optAp}}} \frac{I_k^{\text{optAp}}}{I_k^{\text{ap}}}. \quad (\text{A2})$$

Because the optimal aperture is contained within the aperture used for centroiding, $F^{\text{ap}}/F^{\text{optAp}} > 1$ while $I_k^{\text{optAp}}/I_k^{\text{ap}} < 1$. In the typical case where the background star is much dimmer than the target star, $F^{\text{ap}}/F^{\text{optAp}}$ will be not much greater than 1, while $I_k^{\text{optAp}}/I_k^{\text{ap}}$ can be very close to zero, for example when the core of star k is in the pixel ring and only its wings are in the optimal aperture. Therefore $d_{\text{obs}}^{\text{optAp}}$ can be much smaller than d_{obs} , resulting in a significant overshoot of star k 's position in Equation (A1). This overshoot is particularly likely to happen when star k is outside the optimal aperture, in other words for background stars further from the target star. When star k is brighter than stars in the optimal aperture, including the target star, the overshoot is reduced because the flux in the aperture is dominated by the flux from star k . When star k is in the optimal aperture, the impact on Equation (A1) is much less dramatic and it can provide a very good estimate of the transiting star's position.

REFERENCES

- Batalha, N., et al., 2010a, ApJ, 713(2) L103
 Batalha, N., et al., 2010b, ApJ, 713(2) L109
 Batalha, N., et al., 2012, ApJ, Submitted

- Borucki, W., et al., 2010a, *Science*, 327, 977
- Borucki, et al., 2010b, 713(2) L126
- Borucki, W., et al., 2011, *ApJ*, 728, 117
- Borucki, W., et al., 2011, *ApJ*, 736 19
- Borucki, W., et al., 2012, *ApJ*, 745 120
- Brown, T. M., 2003, *ApJ*, 593, L125
- Bryson, S. T., et al., 2010, *ApJ*, 713(2) L97
- Bryson, S. T., et al., 2010, *Proc. SPIE*, Vol. 7740, 77401D
- Bryson, S. T. and Morton, T., *in preparation*
- Burke, C., *in preparation*
- Caldwell, D., et al., 2010, *ApJ*, 713(2) L92
- Christiansen, J., et al., 2012, http://archive.stsci.edu/kepler/manuals/Data_Characteristics.pdf
- Howell, S., et al., 2012, *ApJ*, 746, 123
- Jenkins, J., et al., 2010a, *Proc. SPIE*, Vol. 7740, 77400D
- Jenkins, J., et al., 2010b, *ApJ*, 724, 1108
- Koch, D., et al., 2010a, *ApJ*, 713(2) L79
- Levenberg, K. 1944, *Quarterly of Applied Mathematics*, 2, 164
- Marquardt, D. W. 1963, *Journal of the Society for Industrial and Applied Mathematics*, 11, 431
- Tenenbaum, P. and Jenkins, J. M., 2010, *Proc. SPIE*, Vol. 7740, 77401C
- Torres, G., et al., 2004, *ApJ*, 609, 1071
- Wu, H., et al., 2010, *Proc. SPIE*, Vol. 7740, 774019